University of New South Wales

Graduate School of Biomedical Engineering

Non-Plagiarism Declaration

z5159985	Whiteman	Eleanor Francine
Student Number	*Family Name*	*Other Names*

BIOM4953	Research Thesis C
Course ID	*Course Name*

26/04/2021	Michael Stevens
Submission Date	*Course Coordinator/Lecturer*

Biomedical Engineering Thesis C: 3D Printing of Accurate Arterial Replicas
Assignment Title

In preparing this assessment task I have followed the Student Code of Conduct. I certify that I have read and understand the University requirements in respect of student academic misconduct outlined in the Student Code of Conduct and the Student Misconduct Procedures, and am aware of any potential plagiarism penalties which may apply. I declare that this assessment item is my own work except where acknowledged, and has not been submitted for academic credit previously in whole or in part. If this is part of a group submission, it represents my equitable contribution and is my own work, except where appropriately acknowledged.

I acknowledge that the assessor of this item may, for assessment purposes:

- Provide a copy to another staff member of the University.
- Communicate a copy of this assessment item to a plagiarism checking service (such as Turnitin) which may then retain a copy of the assessment item on its database for the purpose of future plagiarism checking.

I have retained a copy of this, my assignment, which I can provide if necessary. By signing this declaration I am agreeing to the statements and conditions above.

EWhiteman	26/04/2021
Signature	*Date*

University of New South Wales

BIOM4953

Biomedical Engineering Thesis C

3D Printing of Accurate Arterial Replicas

Author:
Eleanor Whiteman

Student ID:
z5159985

April 26, 2021

Abstract

Cardiovascular disease is the number one cause of death globally, with coronary artery disease being the largest contributor in the category. Geometrically and mechanically accurate arterial replicas are essential in surgery training and planning, as well as validation of imaging techniques and the design and testing of new medical devices. This thesis project proposes a 3D printed metamaterial design to imitate the mechanical behaviours of human arterial tissues to create a compliant and geometrically accurate phantom. Tuning of geometrical parameters of various metamaterial fibre geometries was performed and implemented into ANSYS FEA simulations, and a final double helix-sinusoid combination geometry was able to closely replicate the target atherosclerotic coronary artery stress-strain curve up to 5.5% strain in the longitudinal direction. Additionally, deformations perpendicular to the direction of displacement were significantly reduced compared to designs from previous papers. The final geometry was integrated into tensile testing strips and bifurcation geometry for future 3D printing and testing.

Acknowledgements

I would like to thank my supervisor, Dr Susann Beier, for giving me the opportunity to participate in this research and providing guidance each week. Thank you to Mr Ramtin Gharleghi for his guidance and advice throughout the year. I would also like to thank my friends and family for their incredible support throughout this challenging year.

Table of Contents

List of Figures

List of Tables

Nomenclature

Abbreviations

CVD	Cardiovascular disease
CAD	Coronary artery disease
CHD	Coronary heart disease
FEA	Finite element analysis
FEM	Finite element methods
LAD	Left anterior descending (coronary artery)
SB	Stented bifurcation
CT	Computed tomography (scan)

Variables

E	Young's modulus
d_f	Fibre diameter
d_h	Helical diameter
h	Helical pitch
A	Amplitude
λ	Wavelength
σ	Stress
F	Force
S	Cross-sectional area - note: A is not used to avoid confusion with amplitude
ε	Strain
L	Length
L_i	Initial length

1 Introduction, Background and Aims

1.1 Introduction

Arteries are the blood vessels which carry oxygen- and nutrient-rich blood from the heart to the rest of the body. These arteries have a significant amount of smooth muscle and elastic fibres in their walls to resist deformation from the pulsatile pressure generated by the heart pumping the blood, and consequently have thick, elastic walls in comparison to veins. These walls also have three distinct layers: the intima, which is the innermost wall made up of elastic fibres; the media, which is the middle layer made up of smooth muscle and elastic fibres; and the externa or adventitia, the outermost layer which is made up of elastic fibres and collagen. These arteries vary in size, generally becoming smaller the further away from the heart they become[1]. Without correct arterial function, parts of the body may not obtain sufficient oxygen or nutrients to operate properly, which can lead to other diseases.

Arterial replicas are necessary to educate patients and surgeons on procedures, planning surgeries, validating computational models and imaging techniques, and medical device testing. Current arterial phantoms often prioritise geometrical accuracy over mechanical properties, limiting the usefulness and reliability of these models. Furthermore, traditionally manufactured phantoms are often idealised and representative of a population average, sacrificing the details of individual patients[2].

3D printing is an additive manufacturing technique whereby material is added layer-by-layer to form a three-dimensional part. This process can use a range of techniques to fabricate a finished product, such as fused deposition modelling (FDM), selective laser sintering (SLS) and Polyjet technology. A variety of materials are available to use for printing with different techniques, ranging from polymers to ceramics and metals. 3D printing is capable of fabricating highly complex parts which would otherwise be infeasible using traditional manufacturing methods.

Mechanical metamaterials are composites which usually consist of a stiffer fibre material, and a softer matrix. These fibres are used to change the mechanical properties of the structure under deformations, and as such could be modified to match the curvature of the polymer with soft tissue. Previous models that somewhat replicated the stress-strain curve of coronary arteries produced significant deformations which would cause noise in any tests. Additive manufacturing can be used to print these complex metamaterials from multiple materials.

This paper explores potential geometry that can be used in metamaterials to be 3D printed into accurate arterial replicas to better train surgeons, plan surgeries and validate algorithms.

This report contains background about the context of the project, detailing diseases coronary arteries are affected with and the requirement for arterial replicas. A literature review summarises the major aspects of research conducted in fields relevant to this project and highlights gaps in knowledge. The hypotheses and aims of this research project are stated. The methodology that was followed in this project is given and the research outcomes are presented, with a discussion about the limitations and recommendations for future work.

1.2 Background

This section provides an overview of the context of this project, including a background on cardiovascular disease, coronary artery disease and arterial phantoms.

1.2.1 Cardiovascular Disease

Globally, cardiovascular disease (CVD) is the number one cause of death, accounting for 31% of all deaths in 2016, with an estimated 17.9 million people dying from such diseases globally[3], and one in every four deaths in Australia, with a person dying from CVD every 19 minutes[4]. Figure 1 below presents statistics of the occurrence of CVD in Australia from the 2017-18 National Health Survey.

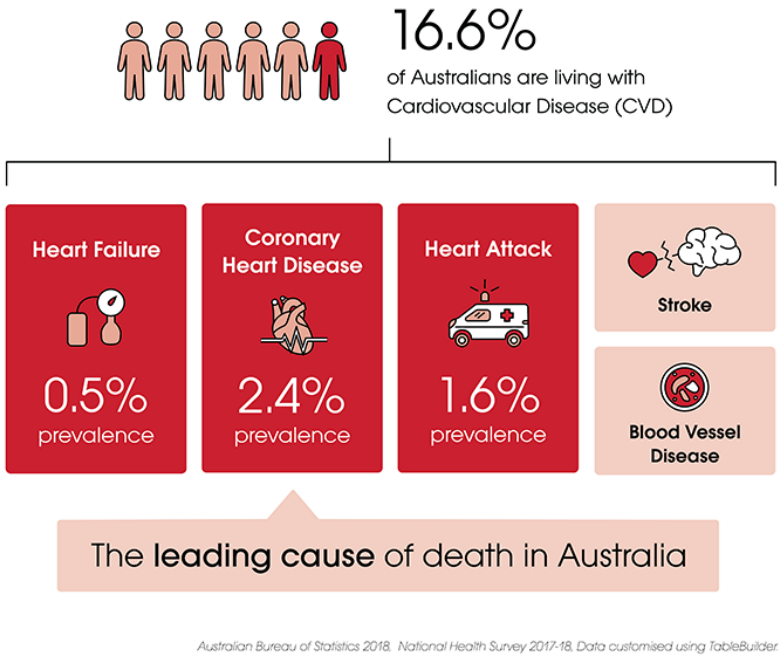

Figure 1: Heart Disease in Australia[4]

Cardiovascular disease refers to a group of diseases which impact the heart and blood vessels. This includes diseases such as coronary artery disease (CAD) (also commonly known as coronary heart disease (CHD)), cerebrovascular disease, peripheral artery disease, rheumatic heart disease, congenital heart disease and deep vein thrombosis[3]. Figure 2 below shows a breakdown of the CVD mortalities in Australia from 2018 into specific diseases, revealing CAD as the most prevalent among them. Most commonly, CVDs present themselves in the form of a heart attack or stroke, which are caused by a fatty buildup in the walls of vasculature supplying blood to the heart or brain[3].

Major causes of CVD death, 2018
Source: AIHW analysis of the National Mortality Database.
http://www.aihw.gov.au/

Figure 2: Breakdown of CVD Mortalities in Australia[5]

1.2.2 Coronary Artery Disease

Coronary artery disease is a condition where plaque, a waxy substance made up of fat, cholesterol, calcium and other blood related substances[6], builds up on the walls of the arteries leading to the heart[7]. This buildup of plaque is called atherosclerosis. The plaque can harden, causing the vessel to narrow and stiffen, which reduces the blood flow to the heart muscles, starving it of oxygen and preventing proper function[8]. Clots can form around this buildup of plaque if the artery wall is damaged, which can completely block blood flow to the heart and cause damage to the heart tissue in the form of a heart attack. A diagram of this can be seen in Figure 3 below.

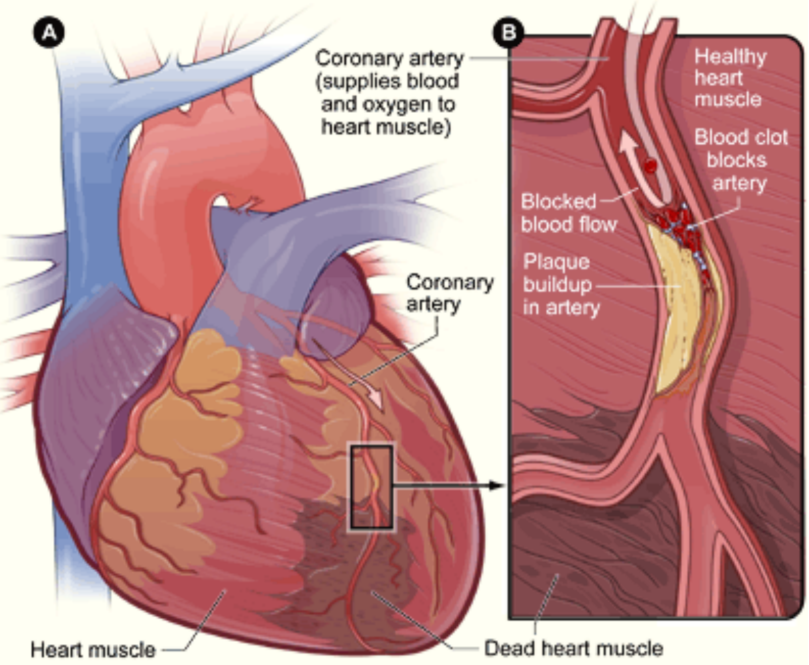

Figure 3: Diagram of a Heart Attack: A) Overview of Heart. B) Cross-Section of Coronary Artery[7]

1.2.2.1 Risk Factors

There are a number of risk factors associated with CAD, many of which can be alleviated through lifestyle changes to prevent the progression of the disease. These risk factors include high levels of "bad" low-density lipoprotein (LDL) cholesterol, low levels of "good" high-density lipoprotein (HDL) cholesterol, high blood pressure, a family history of CAD, diabetes, smoking and obesity[9].

1.2.2.2 Methods of Diagnosis

Often, the first sign of CAD is a heart attack, however pain in the chest, called angina, caused by a lack of sufficient blood supply may also be an early warning sign of this disease[10]. For patients who have symptoms or are at high risk, there are several methods to diagnose CAD, which include performing an electrocardiogram (ECG/EKG), echocardiogram, exercise stress test, chest x-ray, cardiac catheterisation, coronary angiogram or a coronary artery calcium scan using a computed tomography (CT) scan[10].

1.2.2.3 Treatment

Upon being diagnosed with CAD, some patients will be able to make lifestyle changes to their diet, exercise and smoking habits to reduce their risk, whilst others will require medicine to treat high blood pressure or cholesterol[10]. Should the disease have progressed to a point where these treatments are ineffective, surgical treatments may be pursued, such as angioplasty, where a catheter with a balloon is inserted into the artery and inflated to widen the vessel so blood flow can be restored. Angioplasty may be accompanied with the

implantation of a stent to keep the vessel open. Alternatively, medical professionals may decide that bypass surgery (coronary artery bypass grafting or CABG) is more appropriate, which involves using other arteries or veins in the body to redirect blood supply to the heart, effectively bypassing the occlusion[11]. Figure 4 below depicts these surgical treatments.

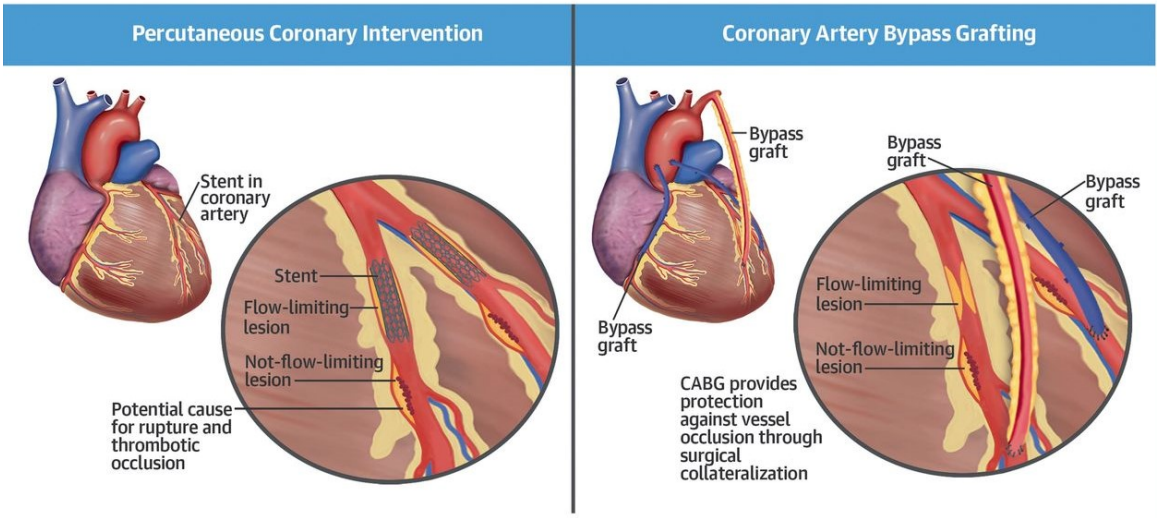

Figure 4: Surgical Treatments for CAD[12]

1.2.3 Arterial Replicas

Although there has been a significant decline in deaths from CAD over the past 30 years[5] due to increased success rates of these treatments and a better understanding of the causes of the disease, further research is required to better understand how existing and proposed treatments impact blood flow within the vessels, and how a treatment would interact within a specific patient's vasculature. Several different methods are currently employed, including computer-based simulations, imaging and bench-top testing.

These physical experiments often require the use of an arterial phantom, which is a medical model replicating the arteries in the human body, ideally mimicking both its geometry and mechanical behaviours under specific conditions[13]. Phantoms can be used to test the fit of a stent within a patient-specific model and assess its suitability to the patient, analyse how blood flows within the vessels and to develop and validate proposed medical devices. They can also be used for surgical training and planning.

A variety of manufacturing methods have been used to fabricate arterial phantoms, however these often compromise on the accuracy of geometry in favour of mechanical attributes or vice versa. Research has been conducted into 3D printing of these arterial replicas in the hope that arterial models can be rapidly fabricated with accurate geometry and mechanical properties, however further development into this area is required.

1.3 Aims

The ultimate aim of this thesis project was to produce accurate arterial replicas which represent a range of disease stages in various populations through 3D printing to solve for the current lack of arterial phantoms which are representative of both geometrical and mechanical properties. This study aimed to find a computational model capable of accurately simulating 3D printed materials for implementation into finite element analysis software. This was be used to computationally simulate and test various geometries of metamaterials in an attempt to replicate the mechanical behaviours of atherosclerotic human arterial walls. The purpose of this was to analyse how geometries impact soft tissue-replicating metamaterials. Finally, this project aimed to result in the implementation of a metamaterial into a coronary artery model to replicate its function and geometry for future 3D printing and testing.

Based on the studies referenced in the literature review (Section 2), it was be hypothesised that the alteration of the internal fibrous geometry of a metamaterial could produce a stress-strain curve similar to soft tissue for large deformations. The geometry was of particular interest, in addition to the fibre radius, amplitude, wavelength and other tunable variables, which were shown to have an impact on a metamaterial's stiffness and strain-hardening behaviours. There was minimal research on the effect of using multiple geometries or lattices to replicate soft tissue behaviour in an arterial phantom. This study aimed to analyse how these geometries may impact the characteristics of such a metamaterial system.

2 Literature Review

A review was conducted on the literature relevant to the proposed research project. This section covers the literature regarding diseased coronary arteries, including locations and properties of disease. Literature regarding coronary artery phantoms was also reviewed, focusing on the manufacturing methods and materials that have been used in the past and are currently being researched. A review of the literature regarding metamaterials was also conducted, specifically looking at their geometries and materials used. Lastly, literature was considered concerning the prediction of material behaviour, including numerical models and computational modelling.

2.1 Diseased Coronary Arteries

This section reviews literature on the locations of disease and physical properties of diseased plaque in patients with coronary artery disease.

2.1.1 Locations of Disease

Singh et al[14] describes how 20% of percutaneous coronary interventions (PCI), also known as angioplasty with a stent, occur at the coronary bifurcation with a lesion, which is a stenosis of greater than 50%. Additionally, stenting is also required in side branch regions, with 50% of left-main and 30% of non-left main bifurcation lesions requiring stents. Latib et al[15] corroborated this information. They described the variations of lesion locations at the bifurcation, which is shown in Figure 5, with “1” indicating the presence and “0” indicating the absence of a lesion. Additionally, they describe the different lengths of lesions and how the bifurcation angle varies from less than 70 degrees to greater than 90 degrees. This indicates that there are significant variations in patient physiology and how a patient can present with CAD, with different degrees of plaque buildup. All of these variations cannot currently be represented in coronary artery phantoms due to restrictions with cost and manufacturing techniques, which may lead to surgeons not being able to sufficiently plan for surgeries.

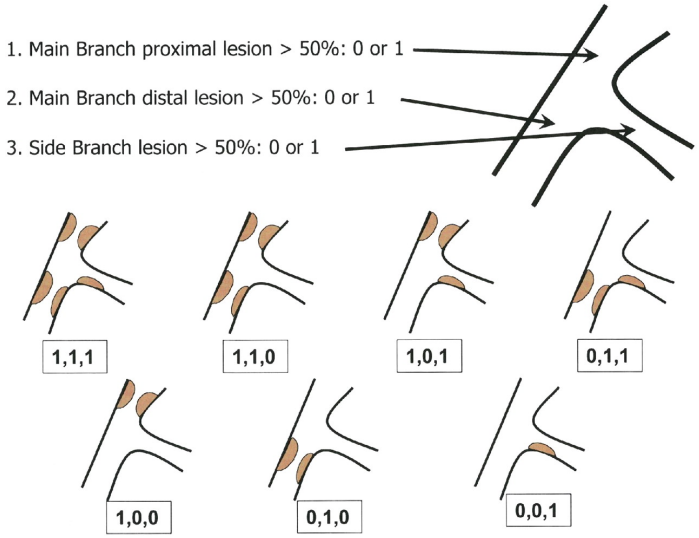

Figure 5: Medina Classification for Coronary Artery Bifurcation Lesions[15]

2.1.2 Physical Properties of Diseased Arteries

In order to accurately mimic the mechanical properties of arteries with disease, it is essential to understand how the diseased tissue behaves.

Holzapfel et al[16] conducted a study on the nonatherosclerotic left anterior descending (LAD) coronary arteries of 13 subjects aged between 64 and 79, with particular interest in the mechanical properties of the individual arterial layers: the intima, media and adventitia. They performed quasi-static uniaxial tests on each test sample in both the axial and circumferential directions, and found that the intima was the stiffest layer, and the media was the softest in the longitudinal direction. They also observed that there was clearly anisotropic behaviour of all three layers, with both the adventitia and the intima being stiffer in the axial direction than the circumferential, and the media exhibiting the opposite behaviour. They hypothesised that this behaviour was due to the orientation of the collagen fibres within the tissues. The ultimate tensile stresses and stretches (in this case represented by λ, not to be confused with wavelength) of each layer are shown in Table 1. The stress-stretch curves they obtained for each layer of arterial tissue are shown in Figure 6. These results may not be accurately representative of actual arteries due to the cutting of the collagen fibres during preparation of the samples, which may have retracted and given altered results, in addition to a small observed sample size, however this study does provide a sufficient estimate of mechanical properties for this project given there is such a large variation in mechanical behaviours of tissue between individuals.

Table 1: Ultimate Tensile Stresses and Stretches for Arterial Layers[16]

	Arterial Layer and Orientation					
	Adventitia		Media		Intima	
	AC (n = 5)	AL (n = 6)	MC (n = 9)	ML (n = 7)	IC (n = 6)	IL (n = 7)
$\bar{\sigma}_{ult}$, kPa	1430.0±604.0	1300.0±692.0	446.0±194.0	419.0±188.0	394.0±223.0	391.0±144.0
$\bar{\lambda}_{ult}$	1.66±0.24	1.87±0.38	1.81±0.37	1.74±0.28	1.60±0.29	1.55±0.40

Values are means ± SD; n, number of specimens, which fractured in the gauge region. $\bar{\sigma}_{ult}$, Ultimate tensile stress; $\bar{\lambda}_{ult}$, ultimate stretch; AC and AL, circumferential and longitudinal adventitia; MC and ML, circumferential and longitudinal media; IC and IL, circumferential and longitudinal intima.

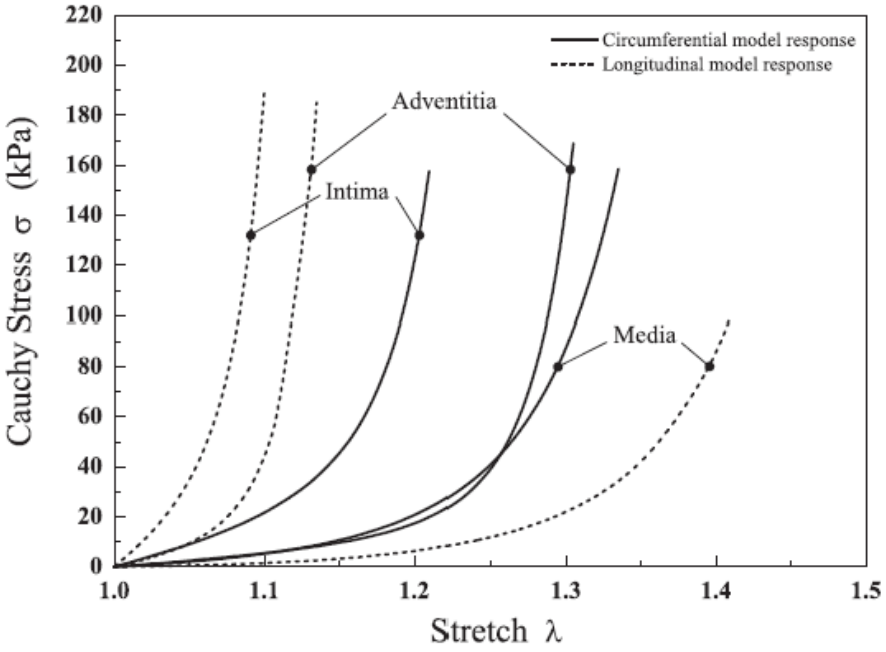

Figure 6: Cauchy Stress-Stretch Curve for Nonatherosclerotic Arterial Layers[16]

Karimi et al[17] published a paper which investigated the role of strain rate on the mechanical properties of both healthy and atherosclerotic human coronary arteries. Figure 7 shows how the stress-strain curve of both types of arteries varies significantly with altered strain rates, yet diseased tissue experiences little mechanical behaviour change up to 20mm/min. This suggests that the load cell chosen to conduct tensile testing experiments must be appropriate in order to accurately control the strain rate and remove additional variables and error. This paper also demonstrated that atherosclerotic arteries are always stiffer than healthy ones.

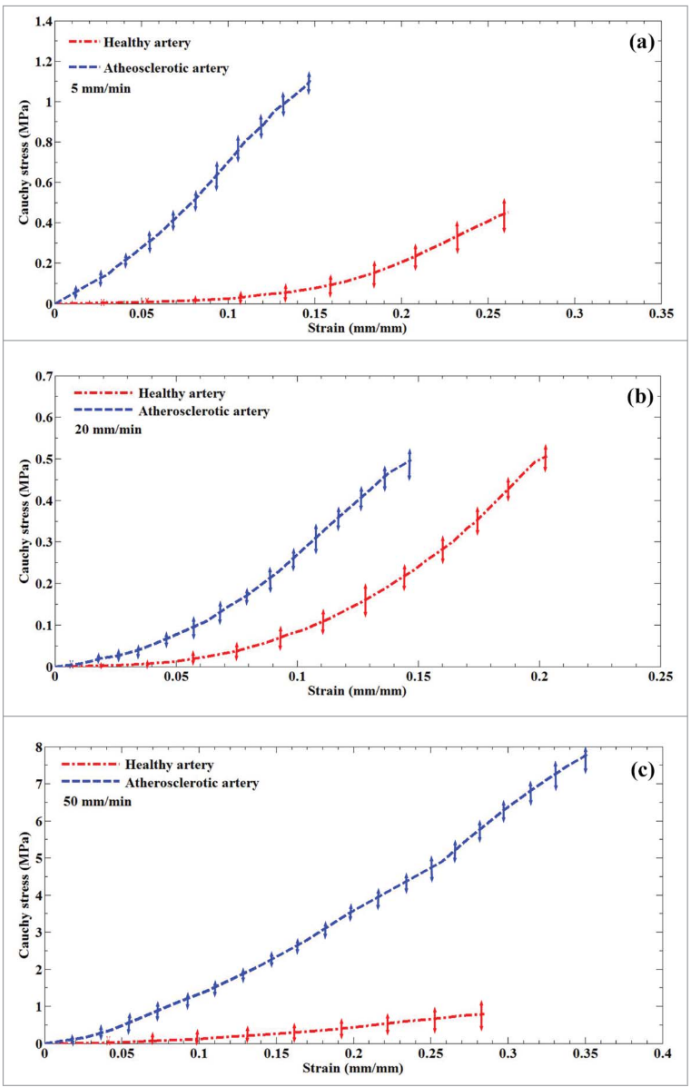

Figure 7: Cauchy Stress-Strain Curve for Healthy and Atherosclerotic Arteries at different Strain Rates[17]

Kural et al[18] performed a study of the longitudinal and circumferential mechanical properties of human coronary arteries using a bi-axial tensile testing machine. Figure 8 depicts their results, which show that the longitudinal direction is stiffer than the circumferential direction in all of their samples. It also demonstrates that the difference between the two directions is highly patient-dependent, and varies greatly with disease condition. Although this data is given in 2nd P-K Stress and Green Strain, the relationships can be utilised to estimate a circumferential target stress-strain curve in the absence of more accurate data.

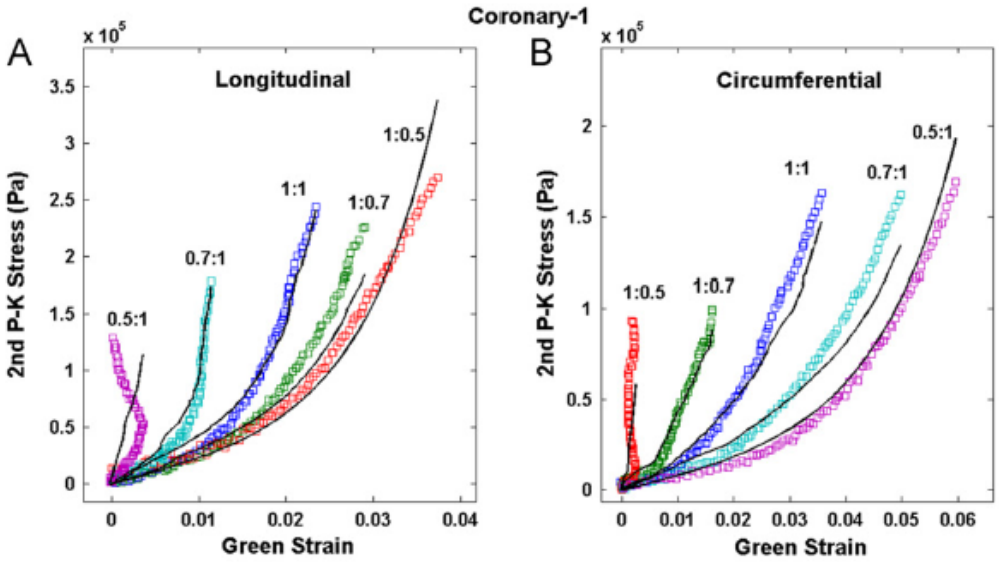

Figure 8: Stress-Strain Curves for Longitudinal and Circumferential Diseased Coronary Arteries[18]

Khanafer et al[19] conducted a study of aortic tissue within 48 hours of sample collection, where they compared various stress-strain relationships. Although this data is not useful to this paper since the study was not conducted using human coronary arteries, the demonstration of the relationships, shown in Figure 9 is able to assist in estimating the circumferential target stress-strain curve.

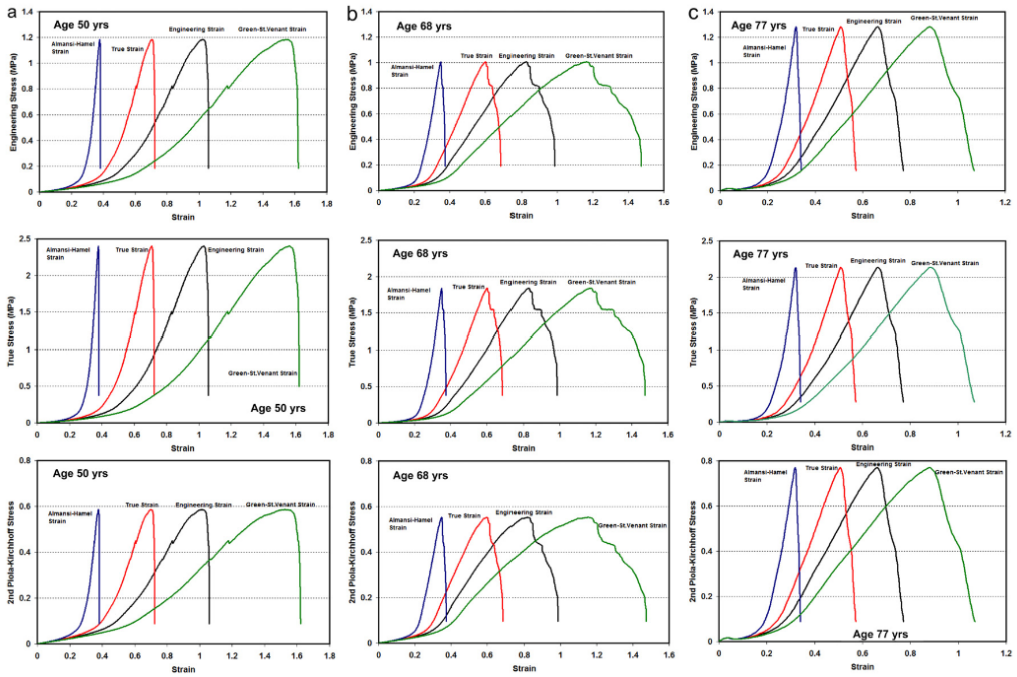

Figure 9: Stress-Strain Curves for Different Ages and Stress-Strain Definitions of Aortic Tissue[19]

Karimi et al[20] published another paper in which healthy and atherosclerotic human coronary arteries were tested uniaxially for their mechanical properties within 5 hours of death to gain results as close to living specimens as possible. This study found that atherosclerotic coronary arteries had a significantly larger stiffness than healthy ones, and experience more stress under lower strain. In this study, specimens were tested at a strain rate of 1mm/min, as it was typical for surgical procedures to apply lower strain rates. They claimed their results may be useful "for designing of new vascular prostheses with appropriate mechanical properties."

Holzapfel et al[21] conducted another study where they observed the mechanical behaviours of atherosclerotic plaques from 107 human samples. They similarly conducted uniaxial tension tests in both the axial and circumferential directions and discovered the arterial tissues behaved anisotropically and had highly non-linear stretch properties, and observed a considerable difference between the mechanical properties of different specimens. Additionally, they found that calcification had a linear property, and that the lowest fracture stress of the fibrous cap occurred in the circumferential direction. On average, they found the adventitia had the highest, and the non-diseased media had the lowest mechanical strength.

Furthermore, Akyildiz et al[22] studied the 3D global architecture of fibrous tissue in atherosclerotic carotid plaques, and discovered that healthy tissue had circumferentially oriented collagen fibres, whilst atherosclerotic plaques had collagen fibres oriented in the longitudinal direction of the blood vessel, which they attributed to a change in the stress and strain distributions upon plaque formation. This highlights that current phantoms do not consider the orientation of the collagen fibres in diseased regions, as they often use a

single material which is not representative of the arterial properties.

Finally, Chai et al[23] studied the mechanical properties of collagen fibres in human carotid atherosclerotic plaques through the use of micro-indentation tests performed over an inverted confocal microscope, and were able to calculate the stiffness of the collagen fibres. They found the ultimate stress of atherosclerotic plaque caps was between 5.2 and 37.5 MPa, and the ultimate strains varied between 0.3 and 1.0. This reflects that there is a large range in mechanical behaviours of diseased tissue across the population, depending on age, disease stage and arterial geometry, which is not represented in idealised phantoms.

2.1.3 Functional Strain Range of Coronary Arteries

Holzapfel et al[21] found in their study that the coronary arteries on average could stretch up to 25% in a longitudinal direction, and up to 26% in the circumferential direction. This data was, however, collected from healthy specimens where the layers of the coronary artery had been separated, and therefore may contain errors. It is expected that atherosclerotic coronary arteries would experience lower levels of strain due to them being stiffer overall.

In their study, Hipper et al[24] identified that arteries experienced a stretch of 5-10% during normal pulse waves from blood flow. They also found that arteries could stretch more than 25% during physiological adjustments. This information can be used to determine the strain ranges that it is desired for a phantom to mimic.

Kural et al[18] also found that strains in the circumferential direction were observed at less than 10% in diseased coronary arteries up to physiological inflation pressures. Additionally, they found that strains of greater than 20% were only found in compliant regions.

2.2 Coronary Artery Phantoms

Coronary artery phantoms are used for the planning of surgeries, medical computational models, algorithm verification and validation, medical device development and patient education[25]. These applications demand high-fidelity, complex, patient-specific models which mimic both the geometry and physiology of human tissue. Unfortunately, current phantoms often prioritise the geometry of phantoms over their mechanical attributes, only representing physiology to less than 3% strain, which could cause errors in the programs they are used to validate or devices they aid in developing. Additionally, these phantoms are often representative of population averages, not representing various disease states or locations, which could complicate surgeries or result in errors.

Phantoms are useful in taking imaging data, which is traditionally presented on a flat screen, and presenting medical professionals or patients with a three-dimensional physical model to better improve their understanding of a surgery or procedure, potentially reducing surgical errors.

2.2.1 Manufacturing of Phantoms

There are a range of manufacturing methods that have been traditionally used to manufacture phantoms. These usually involved developing a tool to mould the part in, which was extremely costly and time consuming[25]. Additionally, as these traditional casting and moulding methods were so expensive and time consuming, idealised, population averaged phantoms were often made, which did not take into account patient-specific properties,

not allowing surgeons to train on models accurate to patients or understand the specific physiology of individuals before surgery.

Brunette et al[26] manufactured their phantom by injection moulding silicone into various tools. This not only meant that the arterial model had to be scaled up so that the tool could be a workable size and the material could be handled, it also meant that the phantom did not have the appropriate mechanical properties to mimic human soft tissue.

Filippou et al[27] also described the limitations of traditional manufacturing methods used to mould phantoms. They stated that these methods were not effective in replicating the complex structure of the human body, especially small blood vessels, due to the requirements for tooling. This highlights the need for the development of another manufacturing method for phantoms that are more representative of actual human physiology.

Additionally, Biglino et al[28] stated that traditional models of arteries were moulded using multiple layers of silicones, polyurethane, latex, or resins, which do not have the appropriate stretch properties to imitate arteries accurately. Additionally, they were manufactured with a uniform wall thickness that did not allow for varied distensibility.

Furthermore, Yazdi et al[29] reviewed the arterial phantom fabrication techniques for phantoms used in flow measurement. They stated that most phantoms were made by producing a 3D model to mimic the blood domain, which is either idealised or patient-specific, usually done through looking at imaging and converting it into a 3D geometry using a computer aided design software. The 3D models were then used to develop casts and the material moulded into them. To manufacture compliant moulds, a male and female mould part were required and a silicone poured in the mould cavity. Alternatively, a dipping technique was used where a phantom was made on the outside of a male mould part, however this could only create uniform wall thicknesses. They found that these moulds were highly sensitive to manufacturing artefacts and wall thickness variations, as compliance dramatically changed with wall thickness. This indicates that a more effective manufacturing method of fabricating compliant arterial phantoms is required.

2.2.2 3D Printing

Dizon et al[30] investigated the characterisation of 3D printed polymers. They noted Polyjet printing technology was highly accurate as it has a high resolution with layers as small as 20μm, its low anisotropy of approximately 2% due to the dense packing of liquid polymer droplets, and low curing energy which allows the part to cure uniformly and create a homogeneous material when required, and noted the ability to use multiple polymers to create complex geometries. Additionally, they noted the use of standards ASTM D638 for tensile test of plastic specimens, ASTM D3039 for tensile test of polymer matrix composite materials, ISO 527 for tensile characterisation of plastics and ASTM D3479 to test the 3D printed polymer matrix materials for tension fatigue. They also investigated the impact of build orientations of the part, shown in Figure 10, revealing that build orientation has a significant impact on a part's mechanical properties, although Polyjet technology is less impacted by different sub-build orientations. This indicates that a variation in part strength is dependent on build orientation and thus care must be taken to select appropriate orientations for manufacturing arterial phantoms so as not to alter the properties. Additionally, they noted that the strength of Polyjet materials degrades over time, revealing that the mechanical properties of the test subject will not be stable

for long-term use. Additionally, they only mention performing uniaxial tensile tests which is not accurate when looking at anisotropic materials, such as metamaterials or 3D printed materials.

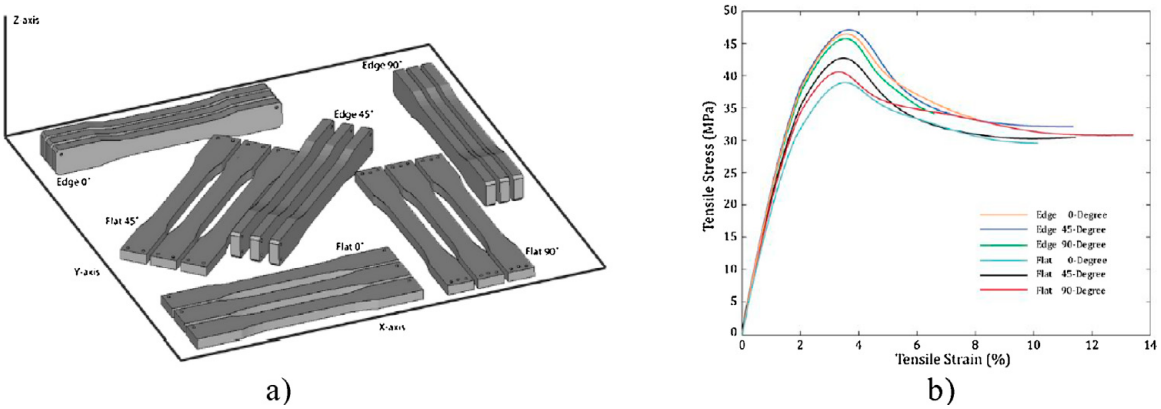

Figure 10: A) Different Build and Sub-Build Orientations. B) Stress-Strain Curve of Materials with different Build Orientations[30]

Toepker et al[31] conducted an investigation into 3D printed coronary vessel phantoms to assess the ability to use these phantoms to quantify stenosis. They used a soft polymer for the vessel wall, and a rigid polymer to simulate the presence of plaque or stenotic lesions, and simulated the motion of the vessel with a cardiac motion simulator to recreate the velocity and motion of the arteries. They found that 3D printed phantoms were able to accurately identify the degree of stenosis from CT scans, and that increasing luminal attenuation decreased the error of stenosis quantification and also increased the image contrast which aided in the recognition of stenosis margins. Although this study used two types of material to imitate vessel properties, it did not account for the difference between the mechanical properties of soft tissue and polymer under high strains.

Biglino et al[28] used polyjet printing to manufacture compliant arterial phantoms with varied wall thickness. They successfully ran prints with this and tested inserting a stent according to surgical guidelines. This can be seen in Figure 11 below. Although this model worked, it only utilised one polymeric material and thus did not represent an arterial system at large deformations. Additionally, they found that models printed in the vertical orientation were more compliant than those printed horizontally.

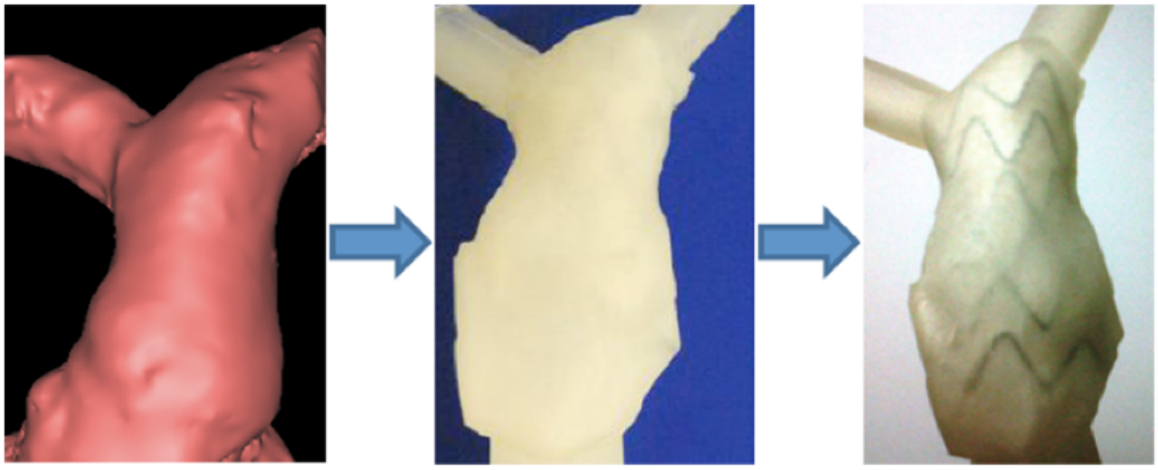

Figure 11: 3D Printed Artery with Implanted Stent[28]

Cloonan et al[32] conducted a study comparing 3D printed materials and traditional elastomers for use with abdominal aortic phantoms. They found 3D printed polymers were comparable to traditional phantom materials. They did not, however, match the function of human soft tissue, which could be improved by utilising combinations of 3D printed materials.

Qian et al[33] studied the application of a 3D printed aortic phantom in detecting paravalvular leak. They 3D printed a metamaterial phantom from CT scans, as shown in Figure 12. They implanted a self-expanding valve prosthesis as per surgical instructions. This showed the feasibility of 3D printing a phantom with tissue mimicking properties and usefulness as a surgical training tool which can assess the suitability of an implant in an individual, however it has not been applied to coronary arteries and further refinement of the metamaterial is required.

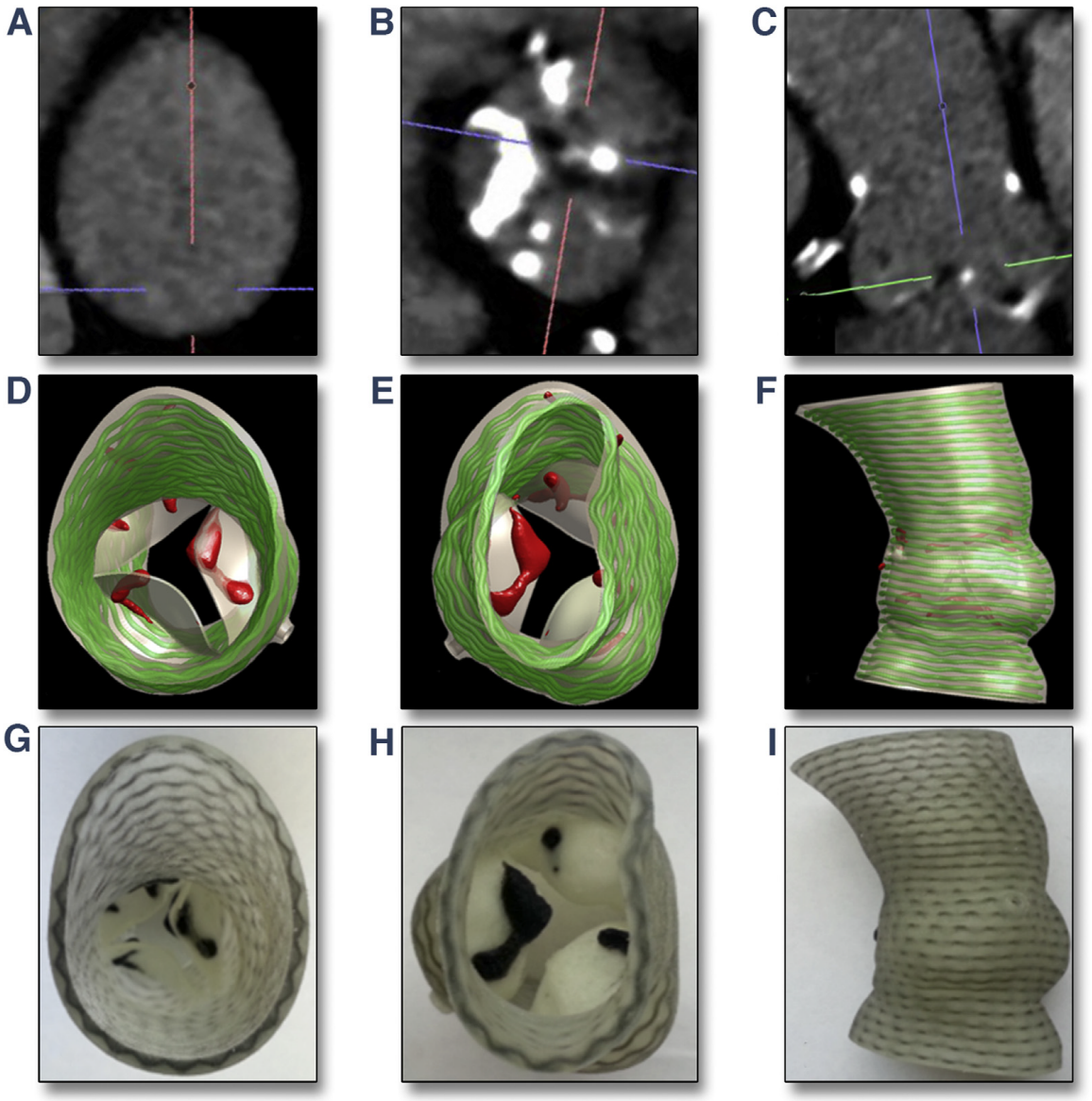

Figure 12: 3D Printed Aortic Phantom. A-C) CT Scans. D-F) 3D Modelling. G-I) 3D Printed Prototype[33]

Although 3D printing is advantageous because of its high accuracy and ability to replicate complex structures, there is also the need for support structure[27], which requires removal and could impact the performance of the part. Furthermore, the surface finish of these parts is not as smooth as traditionally manufactured phantoms, which could have an impact on the interactions with the model, such as shear rates. This may indicate that post-processing is required to 3D printed phantoms to facilitate a better surface finish. Filippou et al[27] also stated that 3D printing could be used directly to physically print a phantom, or indirectly, to rapidly fabricate a mould with complex geometries for use with existing elastomers.

2.3 Metamaterials

A metamaterial is a synthetically fabricated composite material, generated to exhibit properties not usually seen in traditional or natural materials. This usually involves the manipulation of a material's internal structure, and in the context of fabricating accurate arterial replicas using additive manufacturing, metamaterials are intended to alter the mechanical properties of polymers that can be used in 3D printing.

2.3.1 Geometries

Countless combinations of geometries can be employed in metamaterials to exhibit the desired functionalities. Surjadi et al[34] reviewed how the architecture of metamaterials impacted their mechanical performance. They found that metamaterials inspired by cellular materials were often made from a series of interconnected struts, plates of various thicknesses and lengths, or lattices. They also found that most architectures fell into two categories: bending-dominated where deformation occurs through the bending of internal members, and stretch-dominated where deformation occurs through axial tension or compression of its members. Additionally, they outlined the use of origami-inspired metamaterials, where the folding of internal structures is utilised to create intricate geometries that have tunable deformation mechanisms. They also described how metamaterials can be used to gain unique properties, such as negative Poisson's ratios and high bulk moduli compared to shear moduli. They also outlined how additive manufacturing has enabled the development of mechanical metamaterials as it is highly accurate and facilitates the construction of geometries that were not feasible with traditional manufacturing methods. Although this paper describes the possibilities metamaterials are capable of, it does not describe structures which are capable of mimicking human soft tissue under large deformations.

Wang et al[2] investigated the feasibility of mimicking the stress-strain curves of soft tissue such as arterial walls at larger deformations. As seen in Figure 13, their research group observed the effect rigid sinusoidal waves, double helices and interlocking chain fibres had when 3D printed into a soft polymer matrix. They observed sinusoidal waves had a strain-stiffening behaviour up to 4% strain, which was a closer approximation to soft tissue than the strain-softening polymers used. Additionally, they found the double helix structure had a convex stress-strain curve extending past 8% strain, showing that it had potential to mimic elastin-rich tissues. They also found that tuning the geometry of the rigid fibres altered the mechanical properties of the material, with reduced wavelength lowering Young's modulus and increasing strain, and a reduced fibre radius lowering Young's modulus and strain. Wang et al[35] also looked at varying the geometry of a helix to mimic actin filaments, and found altering the fibre radius, helix radius and pitch had an impact on the behaviour of the metamaterials. Although they assessed the feasibility of using this technique to mimic soft tissue strain-stiffening behaviour, they did not obtain material curves which matched those of arteries, nor did they investigate the impact of utilising multiple types of sinusoidal waves or how the fibre affected the mechanical behaviour in directions other than longitudinally.

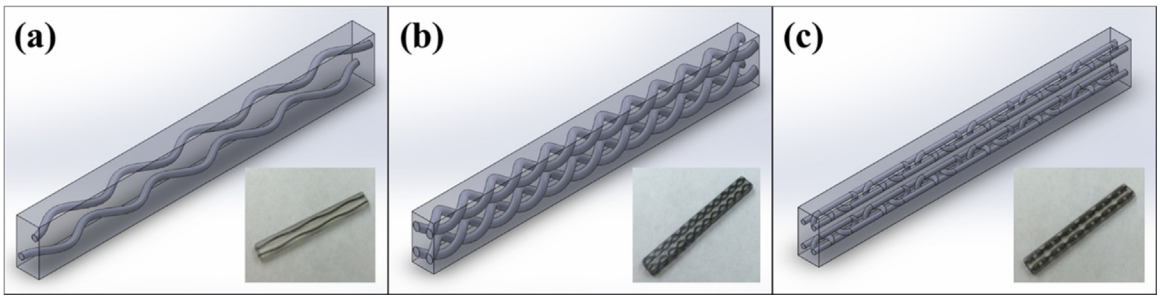

Figure 13: Geometries analysed by Wang et al. A) Sinusoidal Wave. B) Double Helix. C) Interlocking Chain[2]

Bautista[36] implemented a dual material metamaterial with a sinusoidal wave, and studied how tuning the radius, wavelength and amplitude of the fibres impacted the mechanical properties of the material. Their study developed a structure which could imitate the strain hardening behaviour of coronary artery tissue accurately up to 0.1 strain, and observed that the fibre radius impacted the overall stiffness of the material, whilst the wavelength to amplitude ratios impacted the stiffness in addition to the strain-hardening behaviour, with higher ratios resulting in higher stiffness and less strain-stiffening. However, they did not find a material composition which was able to accurately mimic the behaviour of calcified plaque, and found the sinusoidal wave significantly deformed the soft polymer matrix, as seen in Figure 14, indicating that other geometries may gain more favourable characteristics.

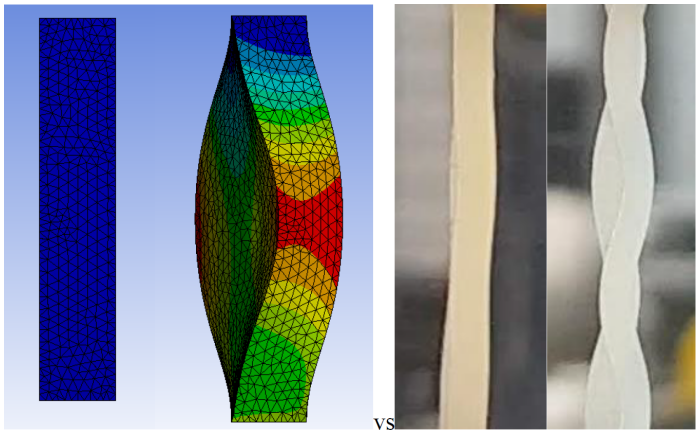

Figure 14: Deformation Behaviour of Simulation and Actual Metamaterial at 8% Strain[36]

As seen in the paper by Qian et al[33], and in Figure 12, sinusoidal metamaterial fibres were positioned circumferentially in the phantom, whereas Bautista[36] proposed that the metamaterial fibres should be longitudinally oriented to match the tissue characteristics. This reflects that further research is required on the optimal orientation to produce the most representative phantom.

Karathanasopoulos et al[37] looked at the function of two-dimensional lattices and their impact on metamaterials. They found that diamond and octagon-shaped planar lattices,

both with and without internal links, had an impact on the Poisson's ratio of materials and their Young's modulus. Additionally, they found that the angle at which the planar lattice is positioned impacts the properties that the metamaterial exhibits. Although this has not been applied to arterial phantoms, it may be able to control the mechanical properties of a phantom to mimic patient-specific models.

Jiang et al[38] published a paper which studied how a simple tubular sinusoidal lattice (Figure 15) could be used in a metamaterial to change the curvature of the stress-strain curve so that it became convex, shown in Figure 16. Although this curvature began after 10% strain, this paper indicates that it is possible to use this geometrical pattern to produce a convex stress-strain curve, and thus suggests that with further tuning, it may be possible to create a geometry with this curvature in the desired region.

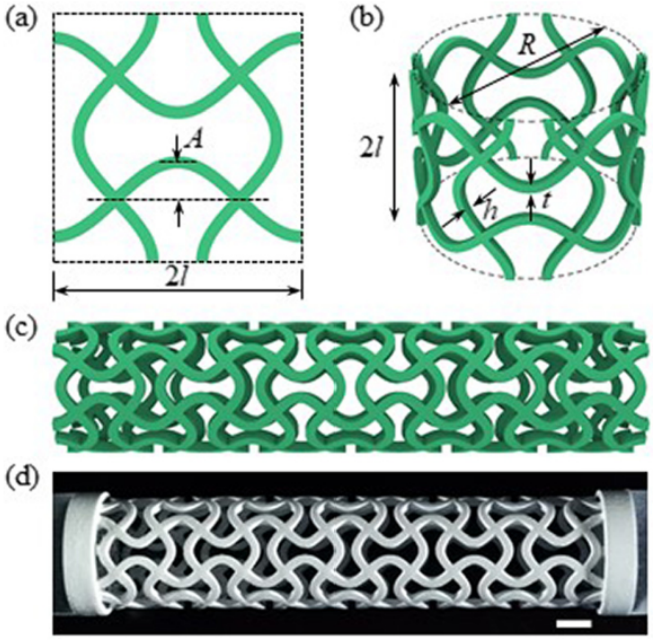

Figure 15: Tubular Sinusoidal Lattice Metamaterial Design[38]

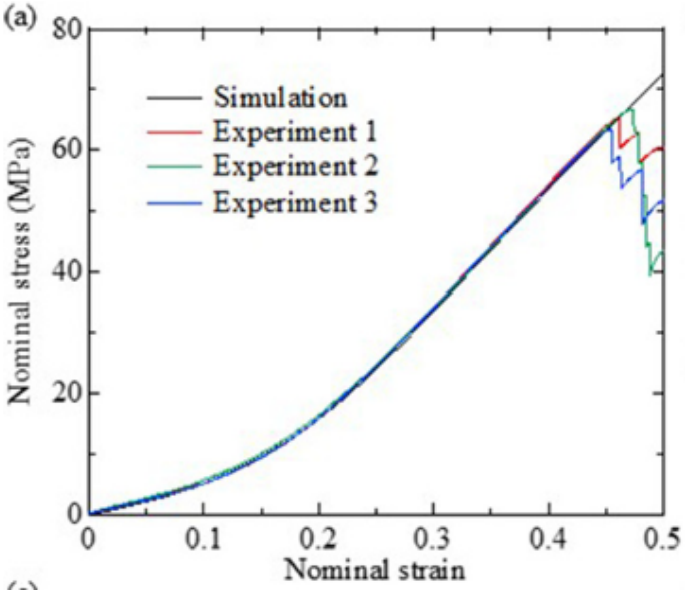

Figure 16: Stress-Strain Curve of Tubular Sinusoidal Lattice Metamaterial Design[38]

Chen et al[39] investigated the effect of how varying the architecture of a sinusoidal lattice impacts the stress-strain curve. As shown in Figure 17, increasing the number of sinusoidal waves in each section can generate a convex stress-strain curve which begins its curvature at earlier strains. This suggests that a modification of this geometry may be useful in replicating the desired coronary artery stress-strain curve.

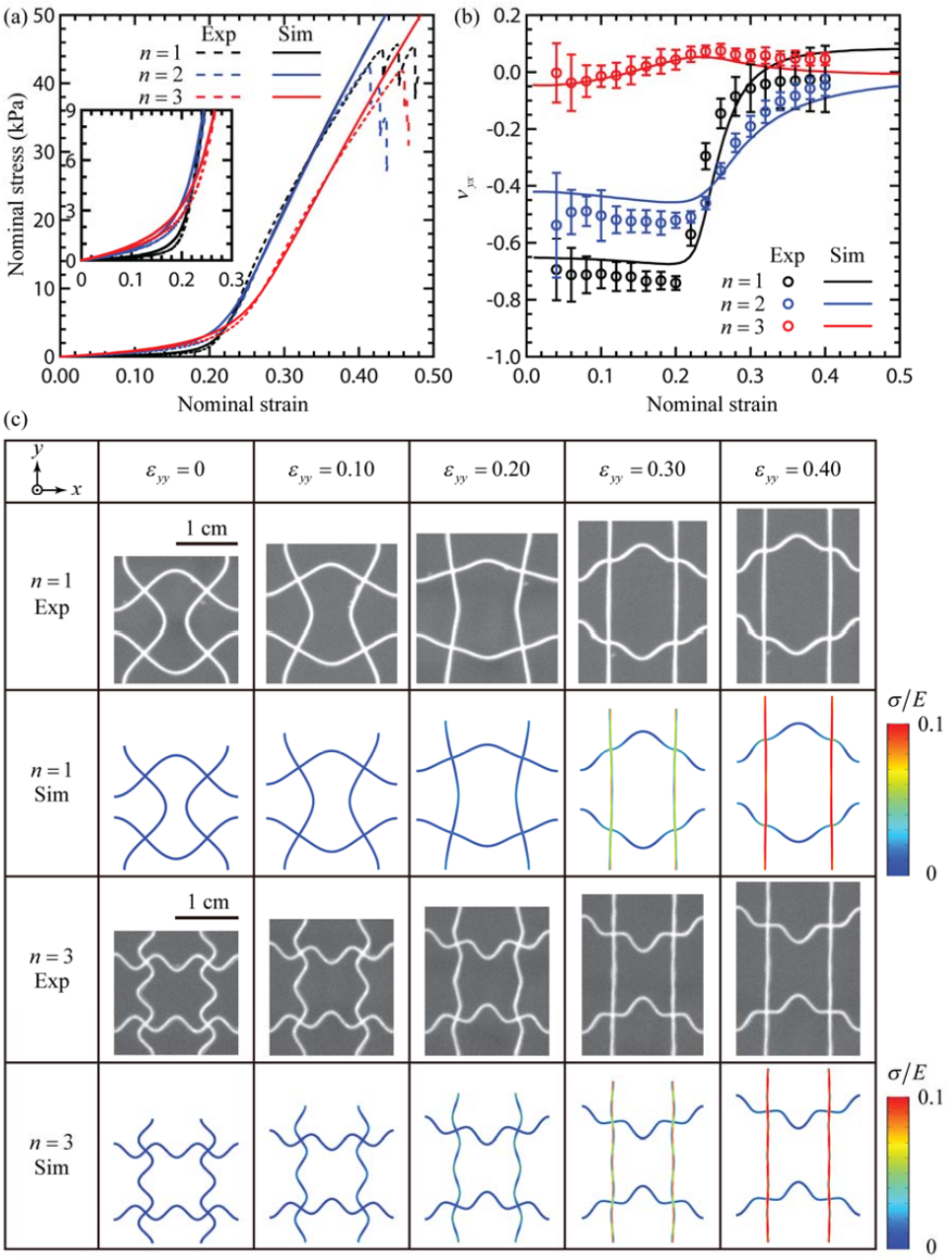

Figure 17: Stress-Strain Curve and Deformation of Complex Sinusoidal Lattice Metamaterial[39]

Additionally, the sinusoidal lattices enable tuning in both the circumferential and longitudinal directions. This may be useful in tuning a geometry which replicates the stress-strain curve in both directions of deformation.

Zhang et al[40] published a paper which focused on the manufacture of 3D mesostructures in advanced materials. They suggested that a kirigami-inspired spring structure, shown in Figure 18 may be tunable to create non-uniform distributions of strain, and thus

it may be extrapolated that the geometry could be tuned to produce a convex stress-strain curve. Additionally, a non-uniform distribution of strain may be useful when developing a geometry which replicates coronary artery tissue, where the mechanical properties vary based on disease location.

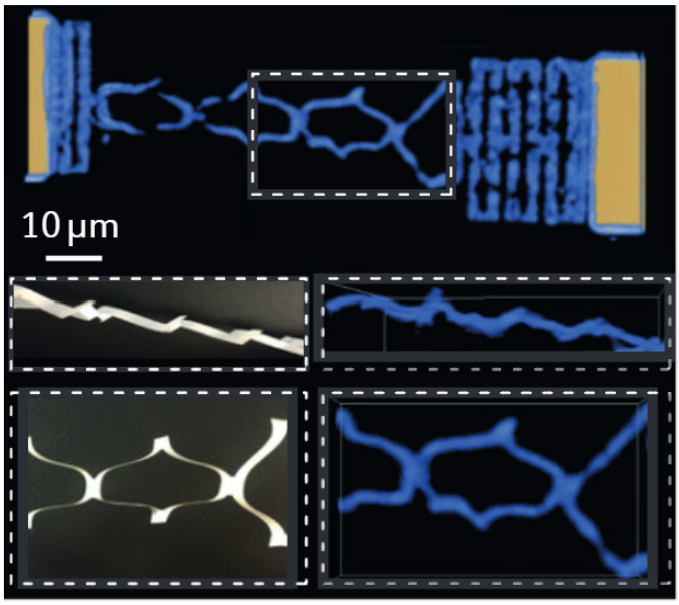

Figure 18: Deformation Behaviour of a Kirigami Inspired Spring[40]

2.3.2 Materials

In their review, Wang et al[25] highlight that soft tissues have an initially convex stress-strain curve, which eventually transitions to concave when the material begins yielding. Polymers used for 3D printing generally have a fully concave curve, which they found could be adjusted by utilising metamaterial structures.

Wang et al[35] conducted another study into metamaterials to mimic soft tissue in polymeric phantoms. The similarity of soft tissues and polymers at low strains can be seen in Figure 19 below, however this also shows the difference between the working strains of the materials. They found that theoretically identical models differed in mechanical behaviour at high strains, indicating that a high resolution of printing is required. Additionally, they printed their metamaterials in TangoPlus and VeroBlackPlus, and found that these materials worked well for mimicking soft tissues as combined metamaterials. However, they did not test the materials past 8% strain due to the breakdown of the interface between the two materials at approximately 9% strain.

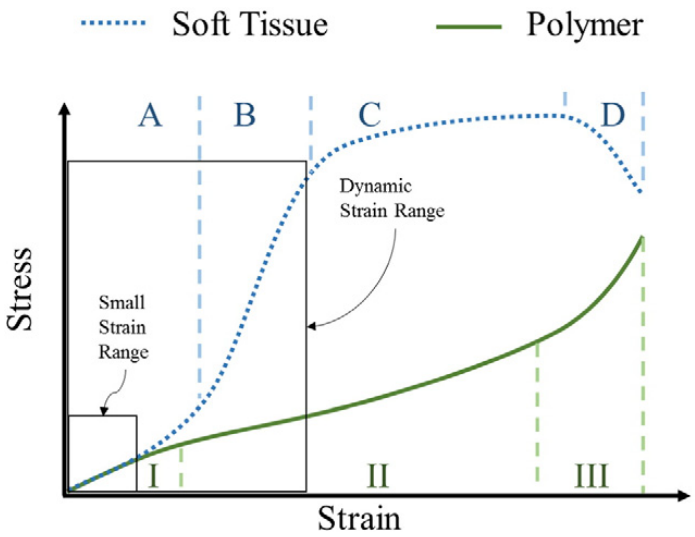

Figure 19: Comparison of Soft Tissue and Polymer Stress-Strain Curves[35]

Bautista[36] found that the materials highlighted in Figure 20 below were also sufficient to approximate arterial tissue as combined metamaterials.

PROPERTIES	ASTM	MULTI-MATERIAL COMPOSITES (VisiJet CR-CL 200** + VisiJet CE-NT)										
Material Name		RCL-ENT-D75	RCL-ENT-D70	RCL-ENT-D65	RCL-ENT-D60	RCL-ENT-D55	RCL-ENT-A90	RCL-ENT-A80	RCL-ENT-A70	RCL-ENT-A60	RCL-ENT-A50	RCL-ENT-A40
Description		Very rigid	Slightly rigid	Rigid	Rigid	Slightly rigid	Slightly flexible	Slightly flexible	Flexible	Flexible	More flexible	Very flexible
Appearance*		Very clear white	Light clear white	Light clear white	Light clear tan	Light clear tan	Medium clear tan	Medium clear tan	Medium clear tan	Translucent tan	Translucent amber	Translucent amber
Tensile Strength (MPa)	D638	19-27	12-16	8-10	4-5	2-3	1.4-1.9	1.3-1.7	.75-1.1	.48-.77	.35-.48	.23-.32
Flexural Strength (MPa)	D790	18-21	12-13	7-7.4	3.9-4.2	1.6-1.9	N/A	N/A	N/A	N/A	N/A	N/A
Flexural Modulus (MPa)	D790	450-750	350-550	150-250	70-180	30-80	N/A	N/A	N/A	N/A	N/A	N/A
Impact Strength (J/m) (Notched Izod)	D256	18-25	22-30	32-52	29-42	74-114	N/A	N/A	N/A	N/A	N/A	N/A
Shore A Hardness, Scale A	D2240	N/A	N/A	N/A	N/A	N/A	86-92	75-85	65-75	55-65	45-55	35-45
Shore D Hardness, Scale D	D2240	70-80	65-75	60-70	55-65	50-60	N/A	N/A	N/A	N/A	N/A	N/A
Tear Resistance (kN/m)	D624	N/A	N/A	N/A	N/A	N/A	44-62	25-32	18-23	11-17	6.6-9.3	6.5-8.5

*Visual approximation. No guarantee that part output will match exactly to software or datasheet values.
** Respectively replaces former VisiJet® CR-WT and VisiJet® CR-CL

Figure 20: Mechanical Properties of Bautista's Selected Materials[36]

2.4 Prediction of Material Behaviour

In developing new materials to have specific characteristics, prediction of the material properties and behaviour is required to reduce the cost of resources and optimise testing. Various models enable the simulation of materials and the prediction of their behaviour.

2.4.1 Prediction of Young's Modulus

Wang et al[35] used various models to predict the Young's modulus of metamaterials. They used the Voigt model to estimate the upper bound of moduli, and the Reuss model to estimate the lower bound. Additionally, they used a micromechanics model to replace the wavy fibres with equivalent straight fibres, after which they calculated the Young's modulus using the Mori-Tanaka model. The estimated modulus was higher than the experimentally obtained one, indicating that this method was not accurate to estimate the behaviour of such metamaterials.

2.4.2 Computational Modelling with Finite Element Analysis

Both Wang et al[2] and Bautista[36] used multilinear kinematic hardening models to simulate the base materials of their metamaterials, using data from uniaxial tests of 3D printed materials. They then implemented this in ANSYS, a finite element modelling software, to estimate the stress-strain curves of the metamaterials. This was compared to data obtained from uniaxial tests of the metamaterials, which it did not match entirely. Although there may have been imperfections in the 3D printed metamaterials, this may also indicate that other material models should be explored to produce more accurate estimates of how the metamaterials will behave.

Kim et al[41] conducted a study comparing several models to predict the behaviour of an elastic material in a computational simulation software, ABAQUS. They initially tested their material with a uniaxial tension test, biaxial tension test and planar shear test, and implemented the data in the software according to the Neo-Hookean model, Mooney-Rivlin model and Ogden models. They found that the Mooney-Rivlin and Ogden models could be used for their elastic material. This has not been applied to approximating metamaterials for coronary artery phantoms, but may prove useful in more accurately approximating them.

2.5 Summary

This literature review has provided an overview of the research in fields relevant to this research project, highlighting that current phantoms are unable to replicate the mechanical behaviours of human coronary arteries due to limitations with traditional materials and manufacturing techniques. These phantoms are representative of idealised populations and sacrifice the geometry and physiology of the individual. Metamaterials have been explored for use in 3D printed phantoms, however not enough geometries have been explored or tuned to successfully replicate the mechanical behaviour of human coronary arteries, with or without disease. Additionally, these metamaterials have been observed to deform unfavourably under large elongations, prompting the investigation of other fibrous geometries. Finally, further investigation into the material models used to simulate the 3D printed polymer materials is required.

3 Methodology

This section covers the methodology that was used throughout this thesis project.

The methods presented in this section of the report were developed to fulfil the aims outlined in Section 1.3.

3.1 Validation of Material Models

The first step in this process was to validate that the material models used for simulating the 3D printed polymers were accurate. This involved researching and exploring various material modelling methods for use in ANSYS. These methods were implemented into ANSYS with the 3D printed material data from Bautista's[36] previous work. Solid blocks of each material were stretched using a deformation of 8% of the block length, and the resulting force experienced at the fixed end was extracted and used to calculate the stress experienced for each strain point. This data was graphed and compared to the input curve to validate whether the material model was appropriate and gave the expected result.

3.2 Validation of ANSYS Simulation

Following the validation of the material models in ANSYS, a validation of the simulation that would be employed over all of the geometries was conducted. A simulation was set up to mimic the simulations of the sinusoidal wave block, of which a simulation had been done by both Bautista[36] and Wang et al[2]. The results from this simulation were compared to those of the previous studies, and the simulation settings were modified until an acceptable match was obtained. Additionally, a validation study was conducted to establish that the chosen mesh for the geometries was sufficient to gain an accurate stress-strain curve. This was done by testing various different mesh and substep settings, such as decreasing the element size, using additional refinement, changing the type of mesh and increasing the number of steps and substeps. When it was observed that the same results were obtained with the altered settings, it was deemed that the initial meshes were acceptable. As Bautista[36] performed an investigation into whether a small sample block of material was equivalent to a tube shape and these simulations were available to check, it was deemed acceptable to use small block simulations instead of larger vessels to reduce the simulation time and size.

3.3 Metamaterial Design and Geometric Modelling

Geometric models of the metamaterials were created using SolidWorks 2019-2020. Various geometries were generated for testing in computer simulations, including a double helix, double helix-sinusoid combination, simple and complex sinusoidal lattices and kirigami springs. Initially, small samples of material ($4\times2\times10$mm) were generated for testing in computer simulations, as demonstrated by Bautista[36], and then larger models of successful geometries were generated for 3D printing and testing. A metamaterial geometry was implemented into a coronary artery bifurcation model to create a 3D printed phantom.

3.4 Simulation using Finite Element Analysis

The geometric models of the metamaterials made in SolidWorks 2019-2020 were imported into ANSYS 2020 R1 as .step files. The Static Structural model was used on these geometries, using a displacement of one end of the block of 8% of it's length, in the longitudinal direction. The same type of mesh was used on each geometry, utilising a mechanical physics preference, using body sizing and refinement. Large deformations were enabled. The boundary and loading conditions were the same as Bautista and Wang et al [2] employed: a fixed support applied to one end, and a tensile deformation of 8% of the length of the specimen applied to the other, as shown in Figure 21. This deformation was chosen to not exceed the yield point of the material where the 3D print delaminates at 9% strain, despite the functional range of human coronary arteries being up to 10% under normal conditions or 25% during physiological adjustments. All models recorded the reaction force at the fixed support, which was used in conjunction with the deformation, obtained from a deformation probe at the deformed boundary, to calculate the stress and strain using Equations (1) and (2) to produce stress-strain curves to compare to arterial data. The chosen target curve came from Karimi et al's publication on the stress-strain behaviour of atherosclerotic coronary arteries[20]. In this round of testing, the simulations were run with A50, A70 and CL as the fibre materials, as these were the best performing from Bautista's[36] paper. Additionally, the geometries were assessed for the amount of deformation which occurred in a perpendicular direction to the applied displacement. Geometries where this displacement was severe were not proceeded with.

$$\sigma = \frac{F}{S} \tag{1}$$

$$\varepsilon = \frac{\Delta L}{L_i} \tag{2}$$

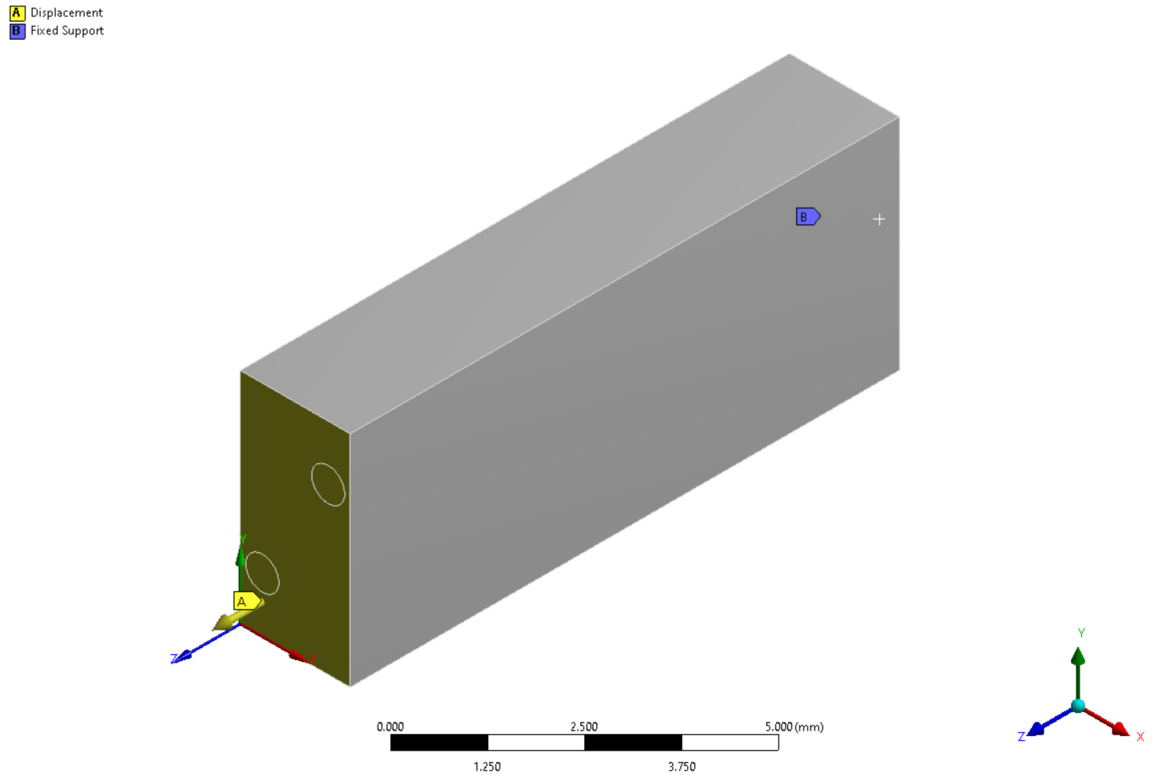

Figure 21: FEA Setup

3.5 Tuning of Geometries

Once initial stress-strain curves were obtained for the various geometries, various tuning parameters were identified, such as fibre radius, wavelength, amplitude, pitch and helical radius, as discussed in Section 2.3.1, and modified within the geometry. These new geometries were set up in the same type of simulation as the previous ones, with the best overall performing fibre material, and their results obtained in the same manner. The relationships between tuning parameters and the convex curve of the material's stress-strain graph were then used to further tune materials which showed evidence of developing a convex curve. For the best performing metamaterial structures, two different mechanical simulations were completed: one for longitudinal behaviour and one for circumferential.

3.6 3D Printing and Optimisation

After the last round of tuning, the best geometry was incorporated into geometry files for tensile testing strips according to ASTM D638 and ISO 527, as recommended by Dizon et al[30]. Additionally, it was incorporated into bifurcation geometry. To optimise files for 3D printing, the 3D models were saved as STL files with a high resolution, as print accuracy is important in capturing the true behaviour of the material. A high resolution of printing is necessary to ensure the accuracy of the part, hence it takes longer to print than lower resolution parts. The fibres and soft polymer matrices were saved as a single file, as the print setup system was unable to superimpose two geometries together. Additionally, all

internal fibres had to be visible on the outer surface so they could be selected to change the material, as it was not possible to select interior structures to change it, thus limiting the types of geometry that could be printed. As noted in Section 2.2.2, the orientation of the part has an impact on its mechanical properties, and thus care was taken to ensure the selected orientation was correct for both function, as well as printing time.

3.7 Resources and Training

The resources and training that were required for the successful completion of this project to meet the aims outlined in Section 1.3 are listed in Tables 7 and 8 in Appendix A.

4 Research Outcomes

In this section, the major findings from this project are presented.

4.1 Validation of Material Model

This section shows the results of the material model validation for the soft NT, hard CL, medium A70 and Medium A50 materials.

4.1.1 Soft NT

First, the material model for the soft NT matrix material was investigated for validation. Many different methods were explored in ANSYS to simulate the material, such as using uniaxial tension data, multilinear kinematic hardening, multilinear isotropic hardening and more. There were many material models that were not able to be employed due to lack of material data, as only tension test data was available. As shown in Figure 22, the most accurate material model for this material was the multilinear kinematic hardening model with a Young's modulus of 10MPa. This curve still did not match the input curve, however it was the closest result that could be achieved within the simulation with the available data.

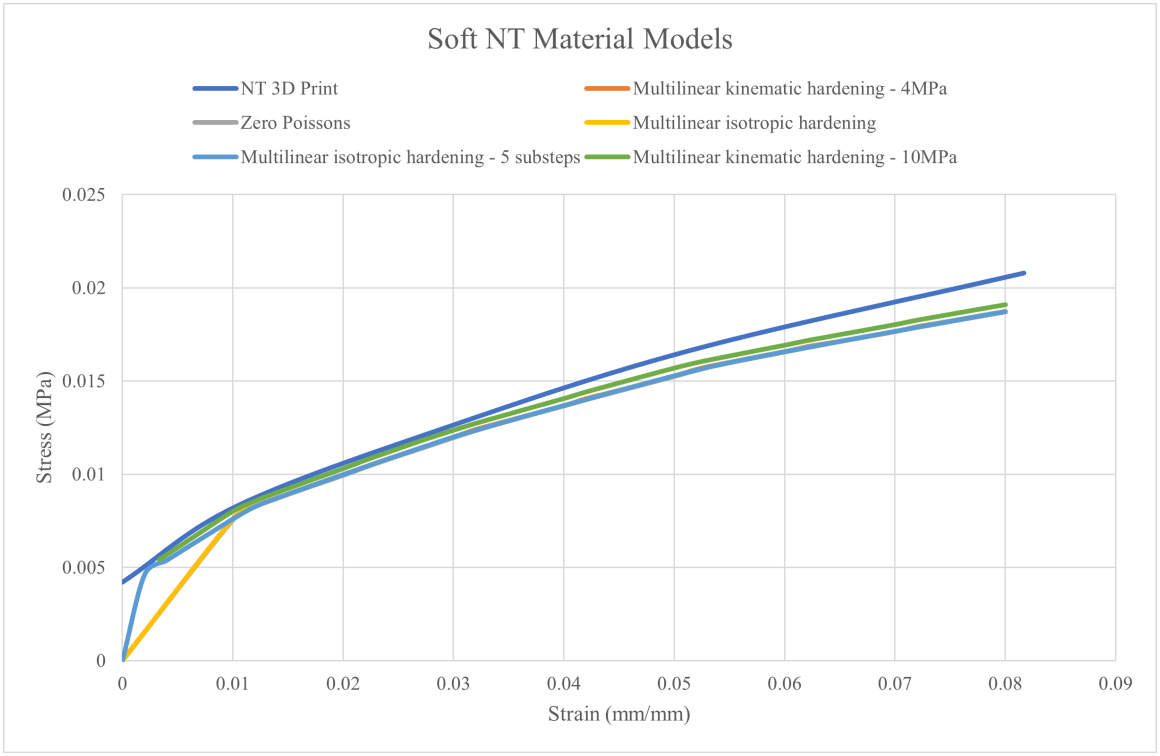

Figure 22: Validation Results from Soft NT Material Models in ANSYS

4.1.2 Hard CL

Similarly to the soft NT material, the hard CL material model was validated by comparing the input data with the results from a simulation of a solid block, as described in Section 3.1. This was explored by changing the Young's Modulus of the multilinear kinematic hardening model, as this was found to be the best model for the NT material. Figure 23 shows that increasing the Young's modulus increases the resulting stiffness of the stress-strain curve up until a point, at which it converges just below the input curve, however increasing the Young's modulus severely impacted simulation time. Consequently, a lower Young's modulus of 3000MPa was selected, as it approximately followed the input curve, whilst maintaining a reasonable computation time for most simulations.

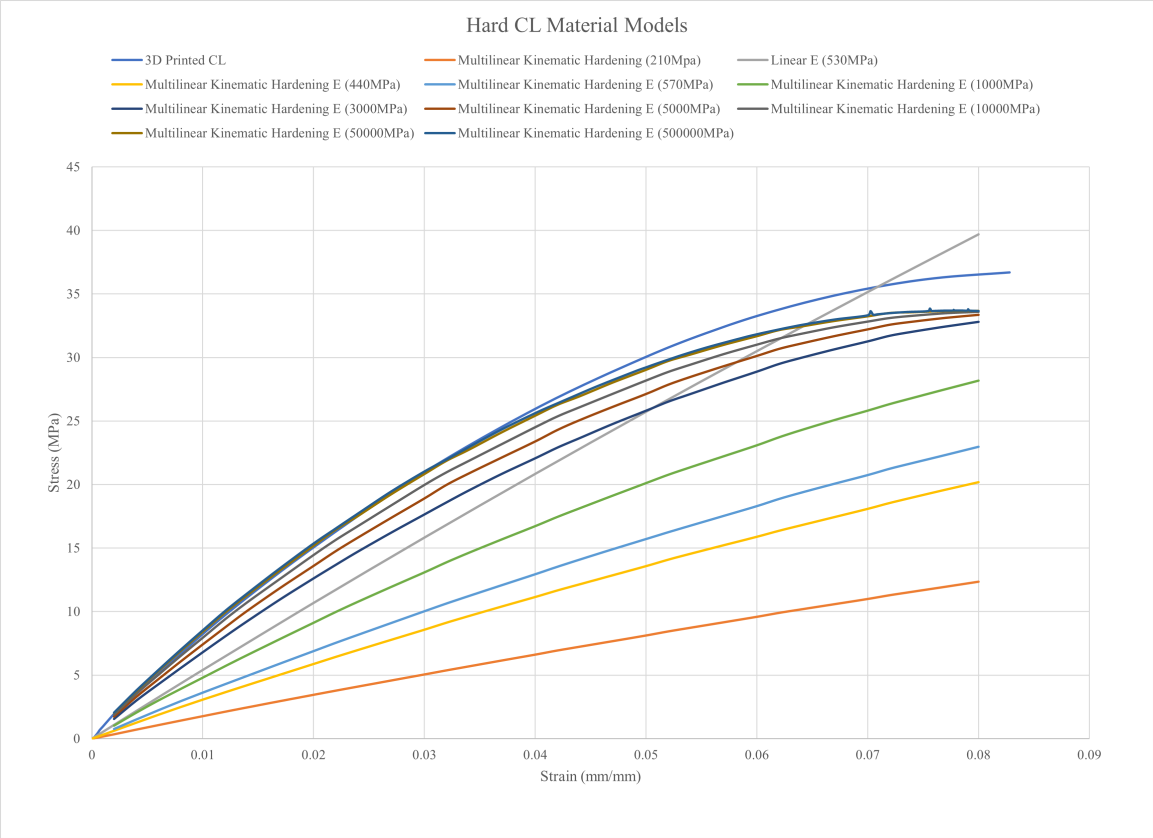

Figure 23: Validation Results from Hard CL Material Models in ANSYS

4.1.3 Medium A70

The same method was used to find an appropriate material model for the medium A70 material. A very good approximation of the 3D print material input data was found using the multilinear kinematic hardening model with a Young's modulus of 50MPa, shown in Figure 24.

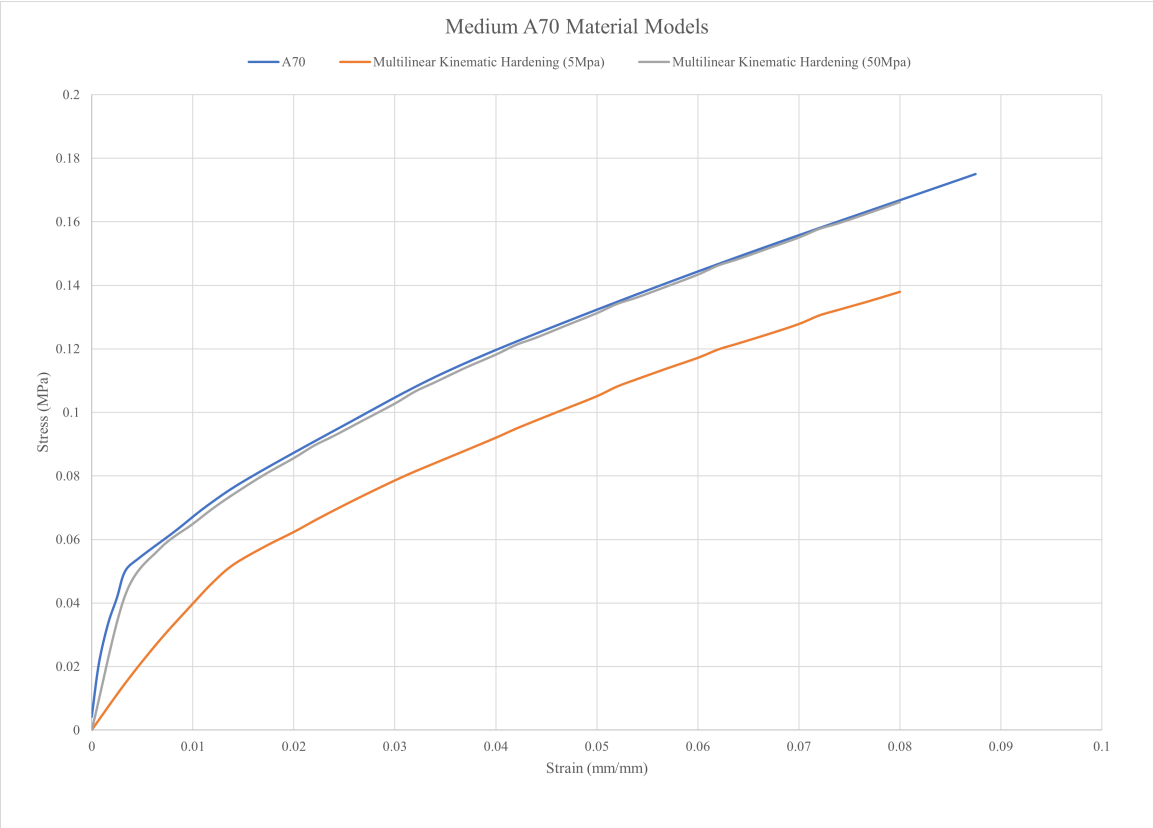

Figure 24: Validation Results from Medium A70 Material Models in ANSYS

4.1.4 Medium A50

Similarly to the A70 material, a very good approximation of the medium A50 material was found using the multilinear kinematic hardening model with a Young's modulus of 50MPa, shown in Figure 25, using the same methodology.

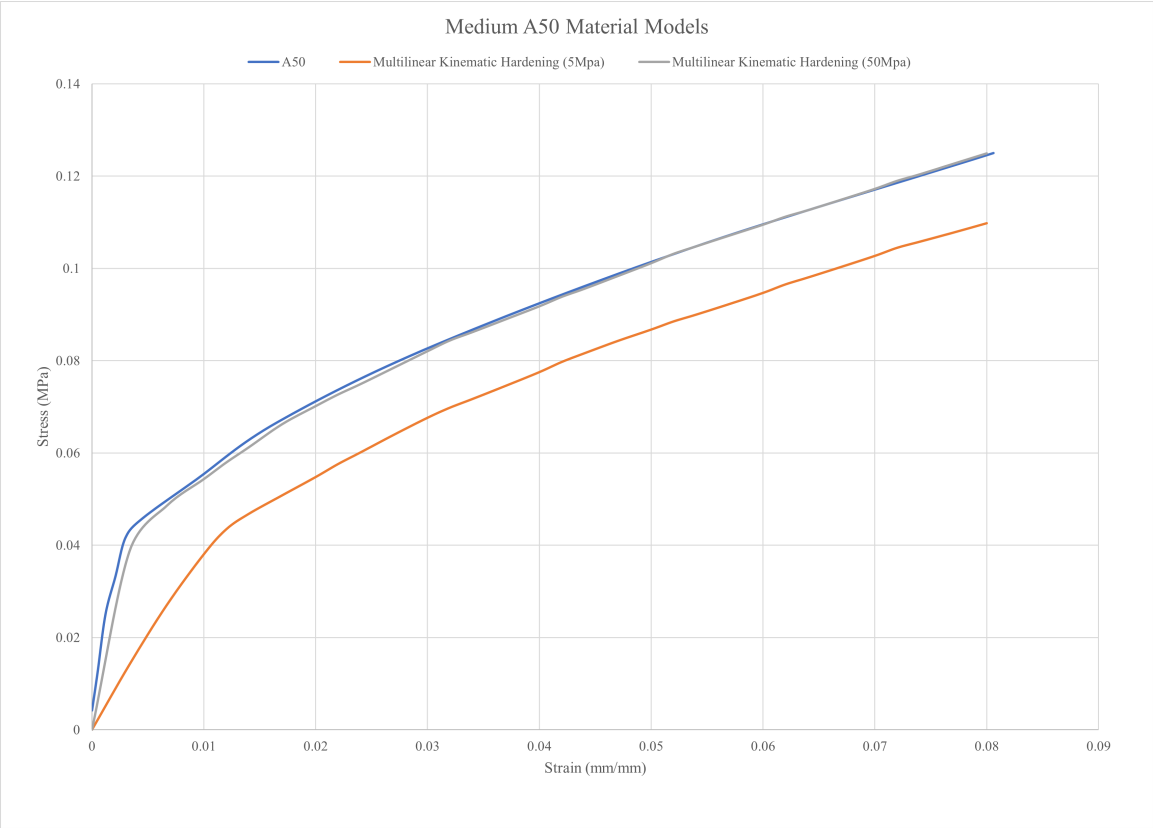

Figure 25: Validation Results from Medium A50 Material Models in ANSYS

4.2 Validation of ANSYS Simulation

This section details the results found from the validation of the ANSYS simulation setup used for this project, executed as described in Section 3.2. An ANSYS simulation was set up with a sinusoidal wave geometry identical to those described by Wang et al[2] and Bautista[36], and a displacement of one end of 8% of its length. Figure 26 shows the simulation from this investigation, Figure 27 shows the simulation from Wang et al and Figure 28 shows the simulation by Bautista. It is noted that stress is located in the same regions, with a similar distribution, however the values of stress are not identical.

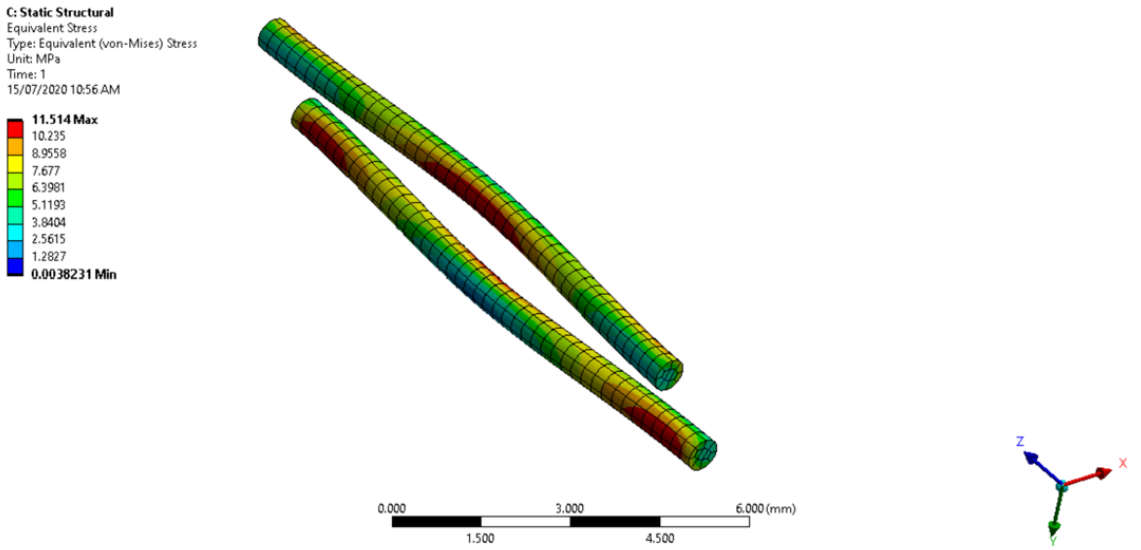

Figure 26: Validation ANSYS Simulation

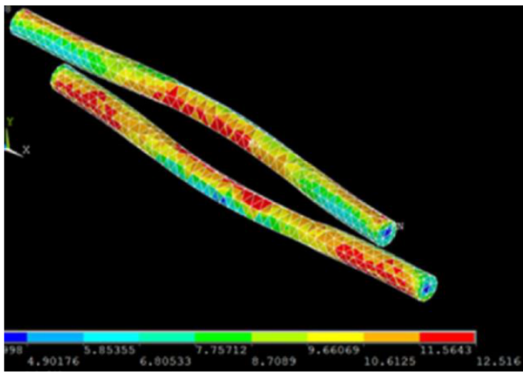

Figure 27: Wang et al's Sinusoidal Metamaterial Simulation[2]

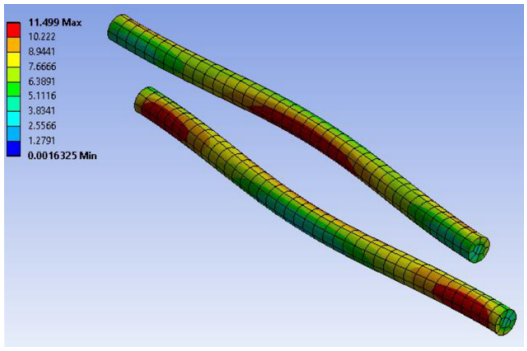

Figure 28: Bautista's Sinusoidal Metamaterial Simulation[36]

Figure 29 shows the graph comparing the results from both Wang et al and Bautista with multiple simulations run in this paper. It shows that both Wang et al and Bautista obtained higher stresses for each given strain, however this may be due to the Vero and Tango material models used by Wang et al not being able to be validated. Additionally, upon further investigation into Bautista's simulations, they used a linear data input to simulate the material, which was not valid. The difference between the simulation run in this paper and Wang et al's may be due to a difference in softwares used to run the simulations.

After many tests involving different meshes, including hex dominant and triangular with various refinements, and different variations in steps and substeps listed in Figure 29, all of the data obtained was identical, indicating that the simulation was reliable and valid when using simpler meshes, which were less computationally intense to run.

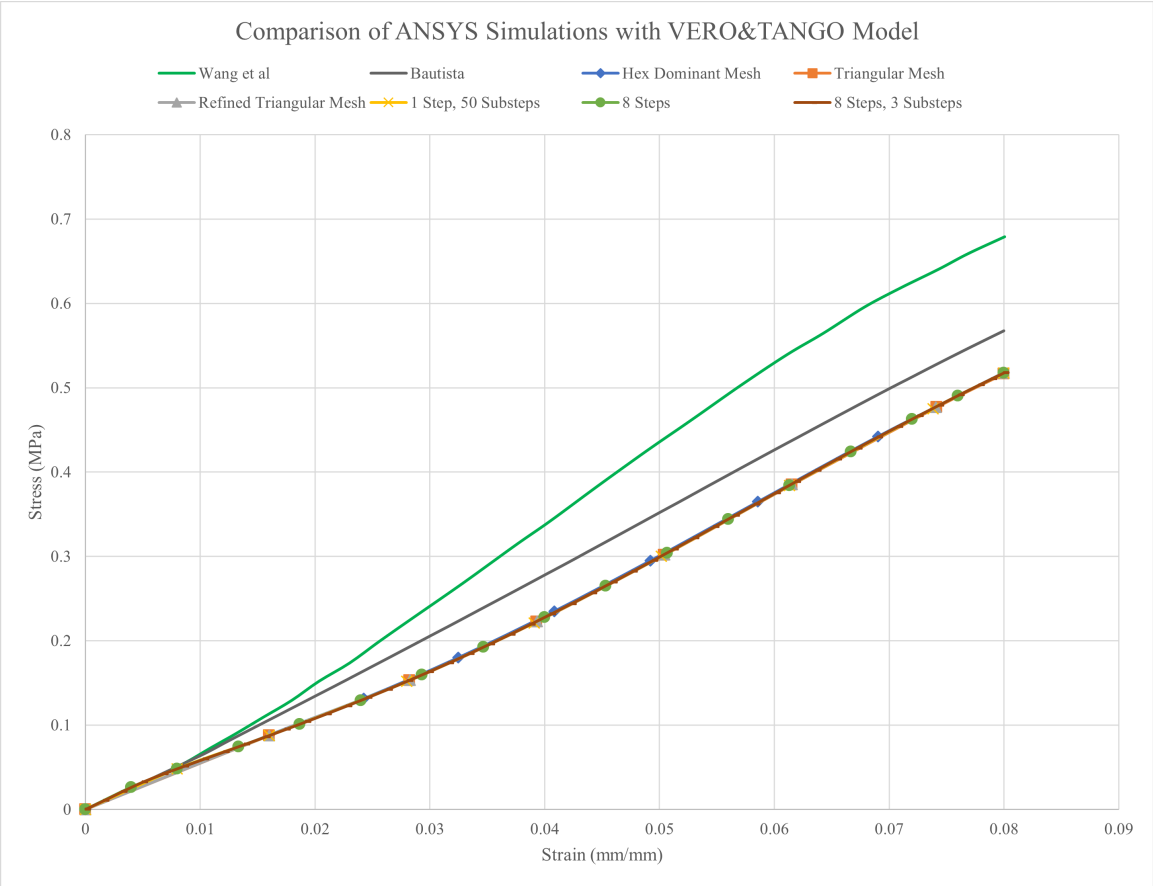

Figure 29: Comparison of ANSYS Simulations to Wang et al[2] and Bautista[36]

4.3 Fibre Material

This section details the results obtained from an analysis of initial geometries, simulated with various fibre materials.

4.3.1 Initial Geometries

The initial double helix geometry that was tested is shown in Figure 30. This double helix had a pitch of 5mm, fibre diameter of 0.4mm, helical diameter of 1.2mm and a spacing between the centre of each helix of 2mm. The original block size was 4mm by 2mm by 10mm.

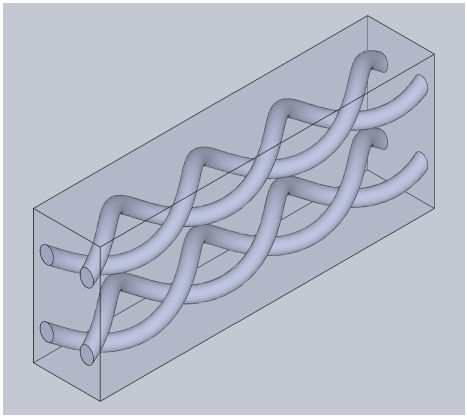

Figure 30: Initial Double Helix Geometry

The initial double helix-sinusoid combination geometry tested is shown in Figure 31. The double helix had the same dimensions as those listed above. The sinusoidal wave had a wavelength of 10mm, amplitude of 0.6mm and fibre diameter of 0.6mm. The spacing between the centre of the double helix and the middle of the sinusoidal wave was 2mm. The original block size was 4mm by 2mm by 10mm.

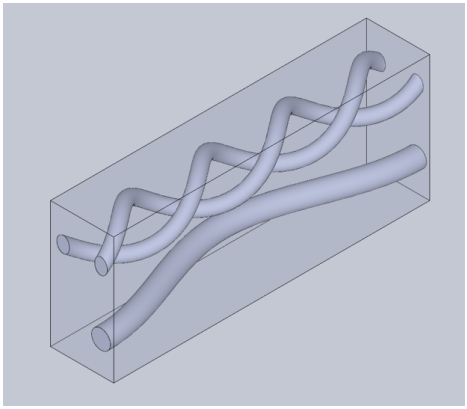

Figure 31: Initial Combination Geometry

The initial simple sinusoidal lattice geometry tested is shown in Figure 32. Each sinusoidal wave had a wavelength of 10mm, amplitude of 1mm and a fibre diameter of 0.4mm. The geometry was constructed such that the sinusoidal waves intersected perpendicularly with half a wavelength between each pair of perpendicular waves. The original block size was 10mm by 4mm by 10mm.

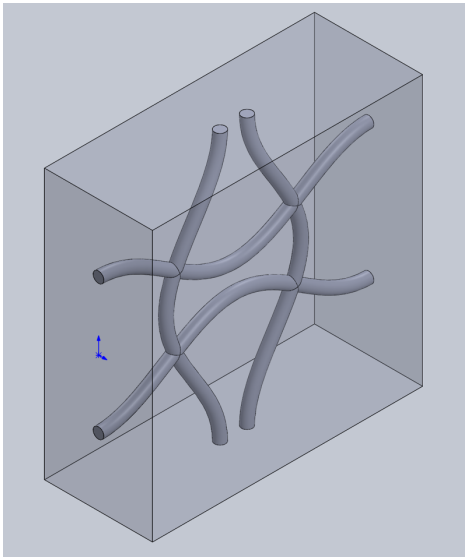

Figure 32: Initial Simple Sinusoidal Lattice Geometry

The initial complex sinusoidal lattice geometry tested is shown in Figure 33. Each sinusoidal wave had a wavelength of 3.3mm, amplitude of 0.5mm and a fibre diameter of 0.4mm. The geometry was constructed such that the sinusoidal waves intersected perpendicularly with one and a half a wavelengths between each pair of perpendicular waves. The original block size was 10mm by 2mm by 10mm.

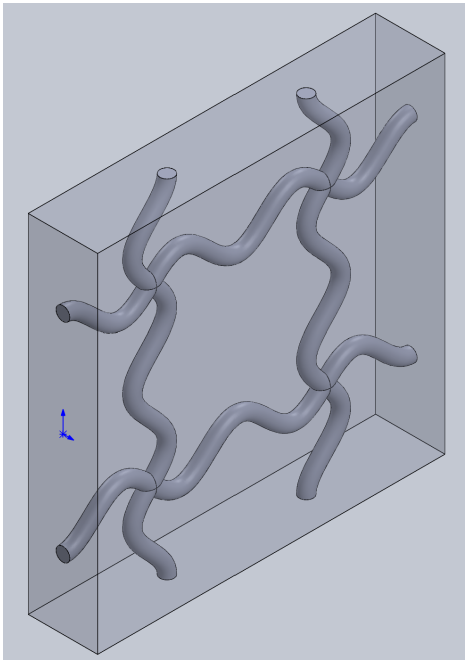

Figure 33: Initial Complex Sinusoidal Lattice Geometry

The initial kirigami spring geometry tested is shown in Figure 34. This geometry was

made with vertical, overlapping sinusoidal waves, each with a wavelength of 6mm, amplitude of 0.5mm and fibre diameter of 0.5mm. This sinusoidal wave was mirrored and repeated 4 times, in a block of size 8mm by 2mm by 10mm.

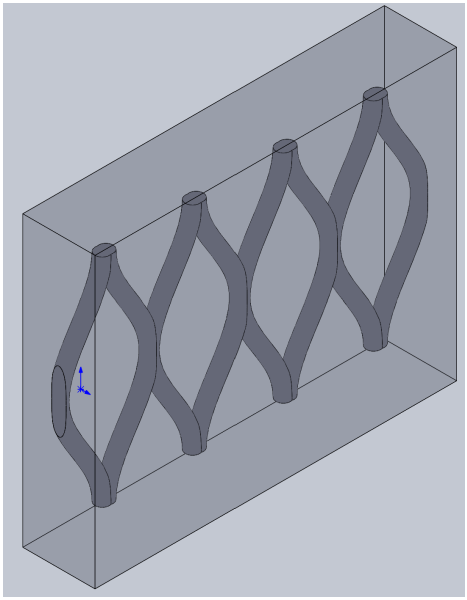

Figure 34: Initial Kirigami Spring Geometry

4.3.2 Fibre Material Results

Each of the geometries listed in Section 4.3 were simulated with 8% strain in the longitudinal direction in ANSYS, using CL, A70 and A50 as the fibre material separately. Figure 35 shows the stress-strain curves for each geometry using the hard CL material as the fibre material. It can be seen that the CL material can develop a large range of curves, including convex curves. Additionally, it has curves both above and below the target curve, indicating that it would be possible to generate a metamaterial that closely follows the target curve.

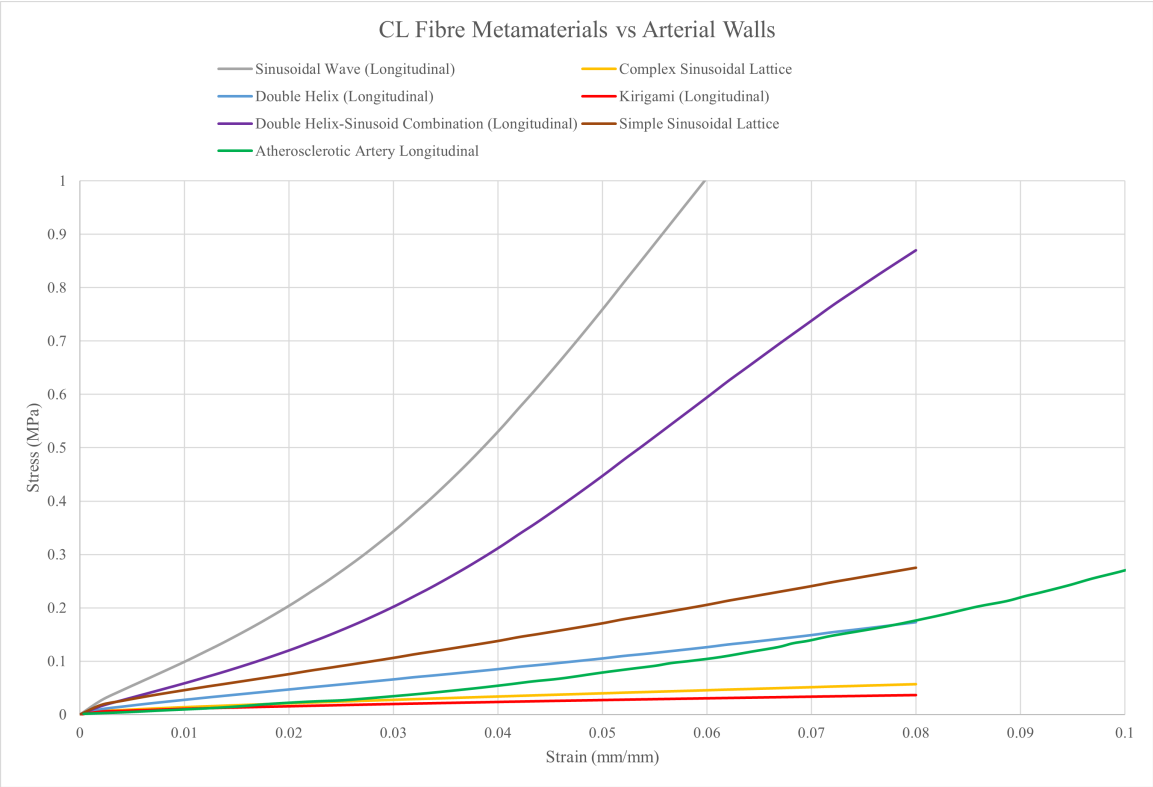

Figure 35: Initial Geometry Simulations with CL as the Fibre Material

Figure 36 shows the stress-strain curves of the initial geometries with medium A70 as the fibre material. As all curves were below the target curve, it indicates that it is unlikely that this material would be effective in increasing the stiffness enough that it could match the target curve.

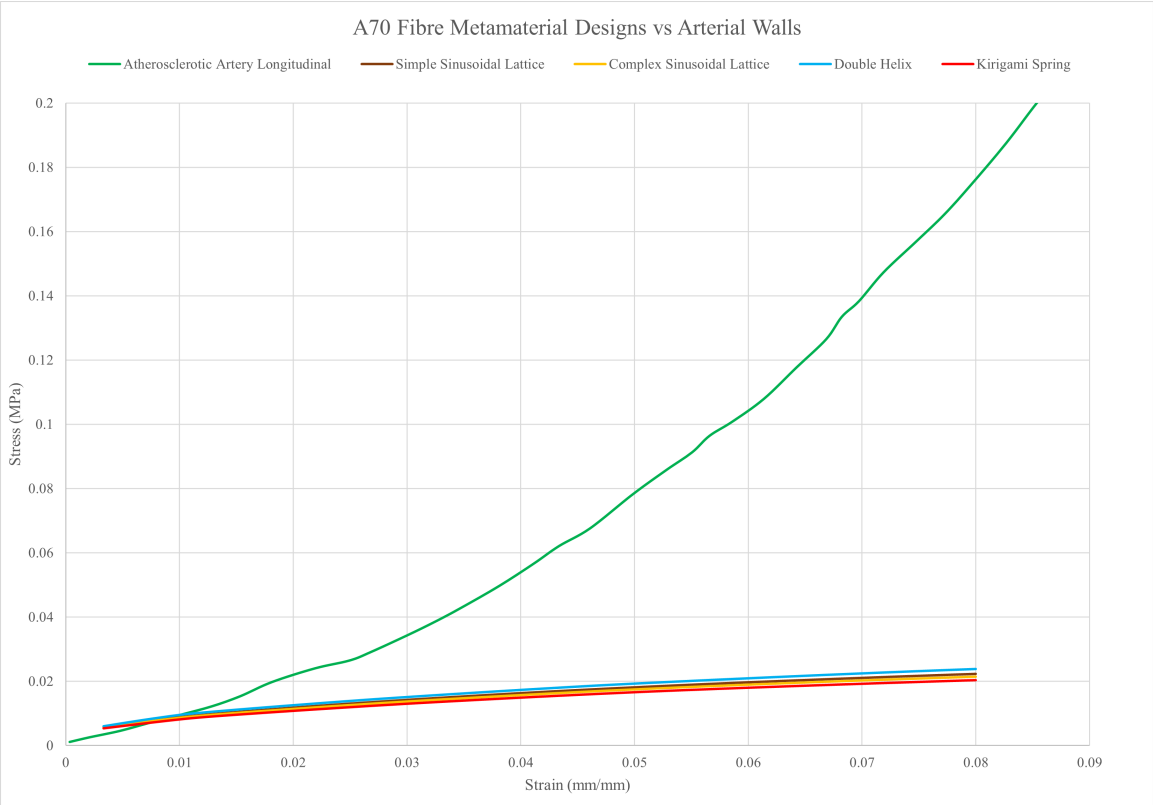

Figure 36: Initial Geometry Simulations with A70 as the Fibre Material

Similarly to the A70 material, the A50 material was also not stiff enough in any of the geometries, which indicates it would not be able to replicate the target curve with any of these geometries. The stress-strain curves with A50 as the fibre material are seen in Figure 37.

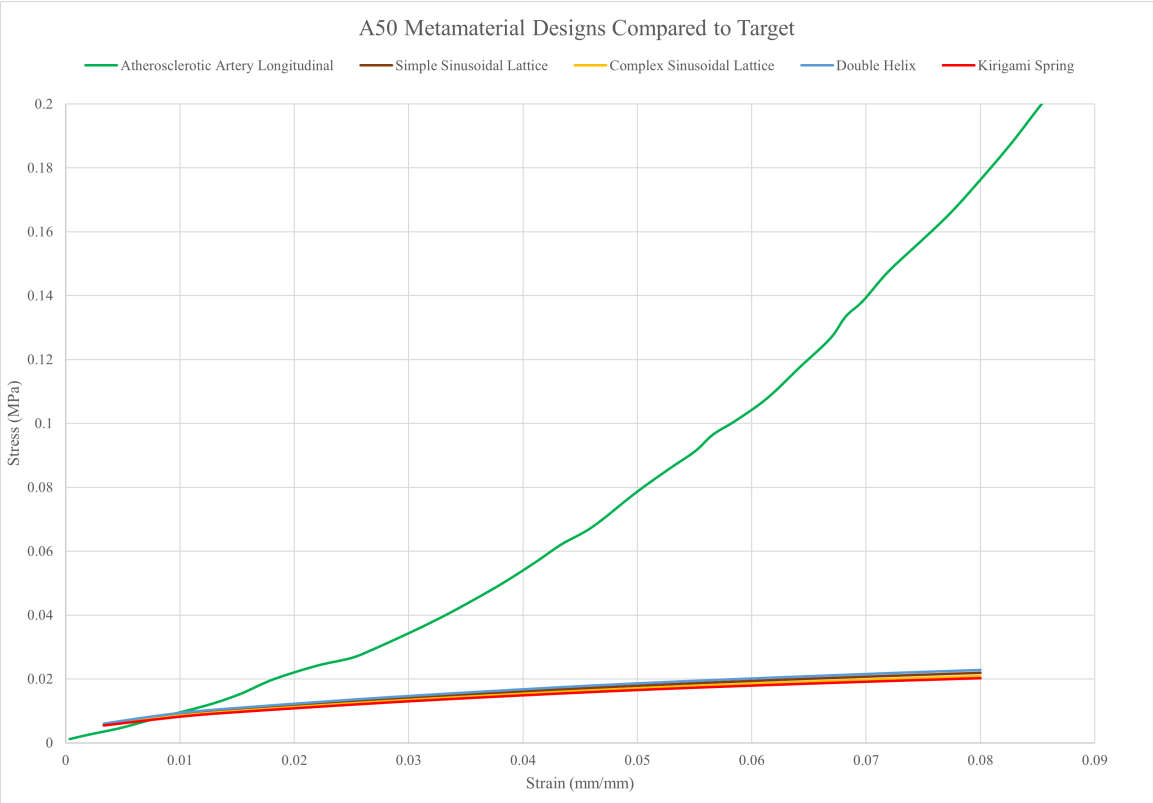

Figure 37: Initial Geometry Simulations with A50 as the Fibre Material

As a result, the hard CL material was chosen to be the most effective at changing the stress-strain curve and developing a convex curvature, and thus was selected to be used in further tests. A50 and A70 were disregarded as they were deemed inappropriate for this purpose.

Additionally, from the CL simulation of the simple sinusoidal lattice, it was noted that the lateral deformation of the block produced dimples in the centre more severe than the complex sinusoidal lattice, seen in Figure 38. Furthermore, as the stress-strain curve was less fitting to the target curve than the complex sinusoidal lattice, the simple sinusoidal lattice was not used in any further simulations.

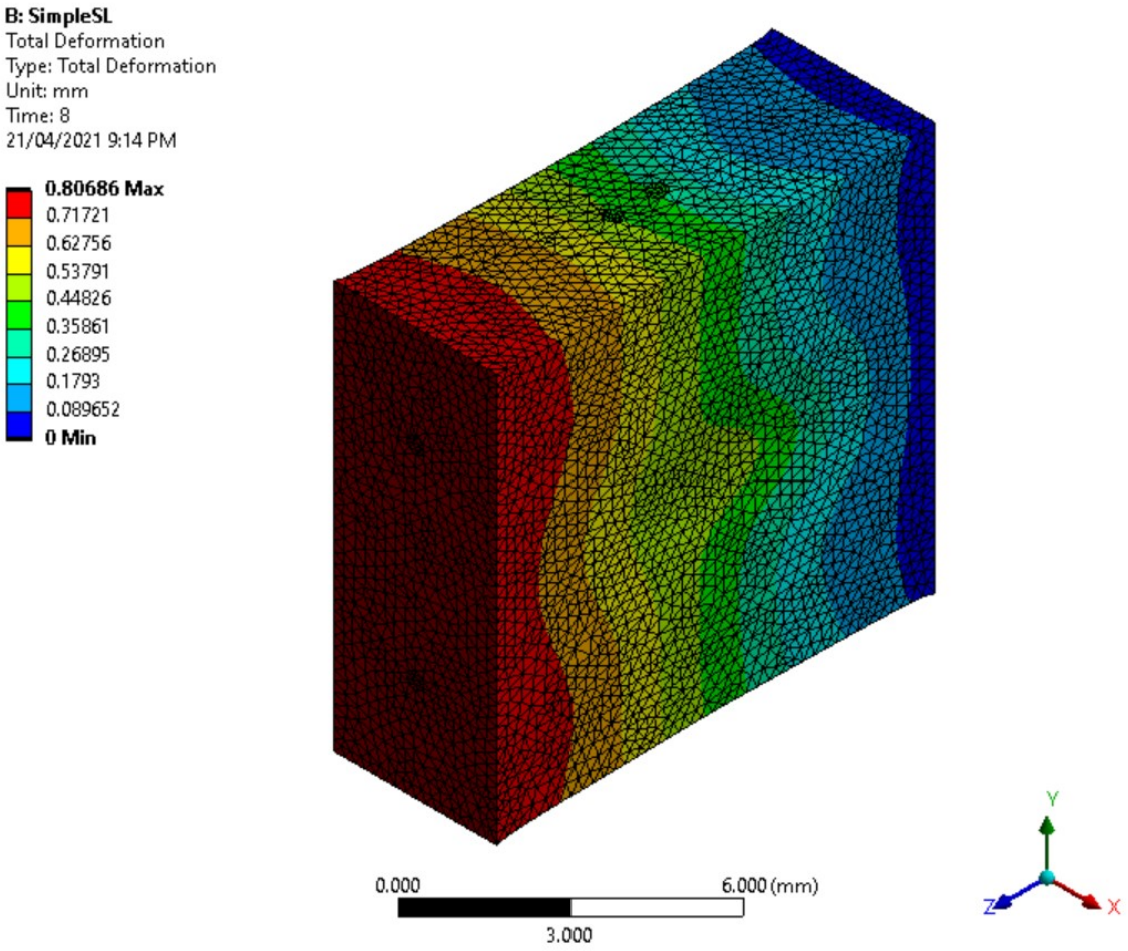

Figure 38: Deformation of Simple Sinusoidal Lattice

4.4 Metamaterial Geometry

This section details the results from tuning the geometries from the previous section, using CL as the fibre material.

4.4.1 Double Helix

In the double helix geometry, the tuning parameters chosen were the pitch, helical diameter, fibre diameter and spacing between fibre elements. The selected tuning parameters are shown in Table 2. The graph of the results can be seen in Figure 39. It can be seen that the double helix can be tuned to create a slightly convex stress-strain curve by decreasing the helical diameter, whilst this also increased the stiffness. Decreasing the fibre diameter, decreasing the pitch and increasing the spacing decreased the stiffness. As such, the double helix had potential to develop a suitable stress-strain curve to match the target.

Table 2: Double Helix Tuning Parameters

Name	Pitch (mm)	Helical Diameter (mm)	Fibre Diameter (mm)	Spacing (mm)
Base (DHp5df0_4dh1_2sp2)	5	1.2	0.4	2
DHp2_5df0_4dh1_2sp2	2.5	1.2	0.4	2
DHp5df0_4dh0_7sp2	5	0.7	0.4	2
DHp5df0_2dh1_2sp2	5	1.2	0.2	2
DHp5df0_4dh1_2sp3	5	1.2	0.4	3
DHp2_5df0_4dh0_8sp2	2.5	0.8	0.4	2
DHp2_5df0_2dh0_8sp2	2.5	0.8	0.2	2
DHp2_5df0_3dh0_8sp2	2.5	0.8	0.3	2

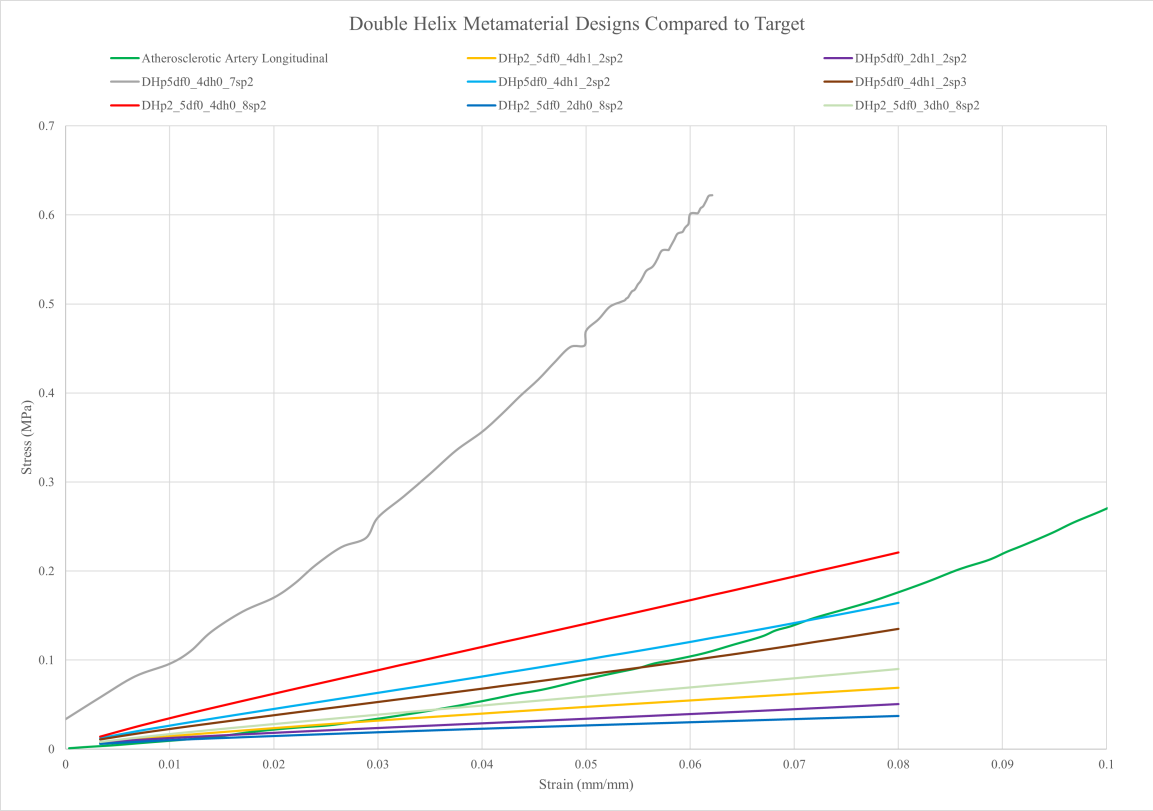

Figure 39: Geometry Tuning Simulations for Double Helix

Figure 40 shows the total deformation of the most fitting double helix curve (DHp2_5df0_4dh1_2sp2). It should be noted that the deformation in the x-direction has some noise, however is significantly lower than the deformation created from the sinusoidal wave geometries in previous papers.

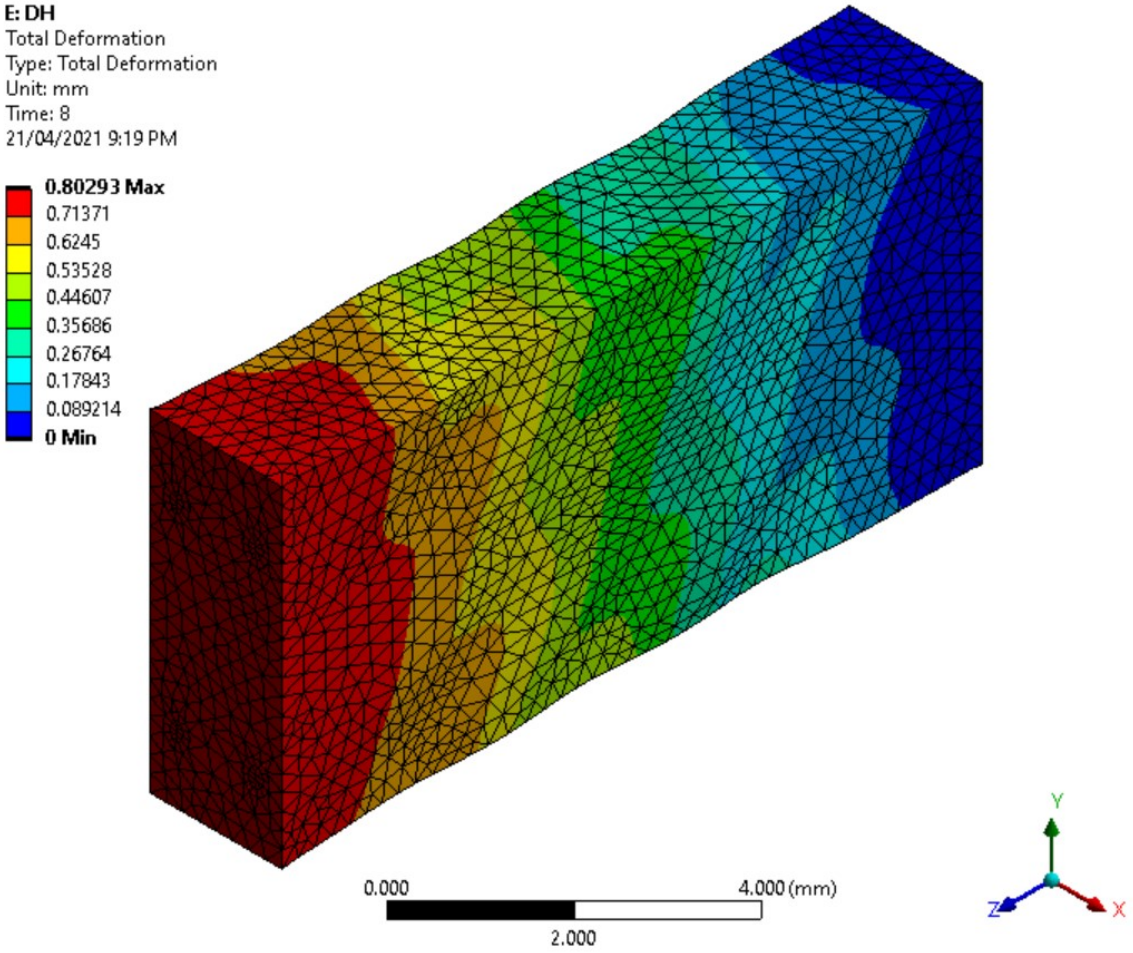

Figure 40: Total Deformation of Final Tuned Double Helix Geometry

4.4.2 Complex Sinusoidal Lattice

In the complex sinusoidal lattice geometry, the tuning parameters chosen were the wavelength and amplitude of the sinusoidal waves, and the fibre diameter. The selected tuning parameters are shown in Table 3. The graph of the results can be seen in Figure 41. It can be seen that decreasing the amplitude and wavelength of the sinusoids increased the stiffness, and decreasing the fibre diameter decreased the stiffness. Despite implementing these tuning parameters, there was no evidence that the stress-strain curve would become convex, and as such the complex sinusoidal lattice was classified as inappropriate for the purpose of creating 3D printed phantoms.

Table 3: Complex Sinusoidal Lattice Tuning Parameters

Name	Wavelength (mm)	Amplitude (mm)	Fibre Diameter (mm)
Base (CSLw3_3a0_5df0_4sp5)	3.3	0.5	0.4
CSLw2_2a0_5df0_4sp3_3	2.2	0.5	0.4
CSLw3_3a0_5df0_2sp5	3.3	0.5	0.2
CSLw3_3a0_25df0_4sp5	3.3	0.25	0.4

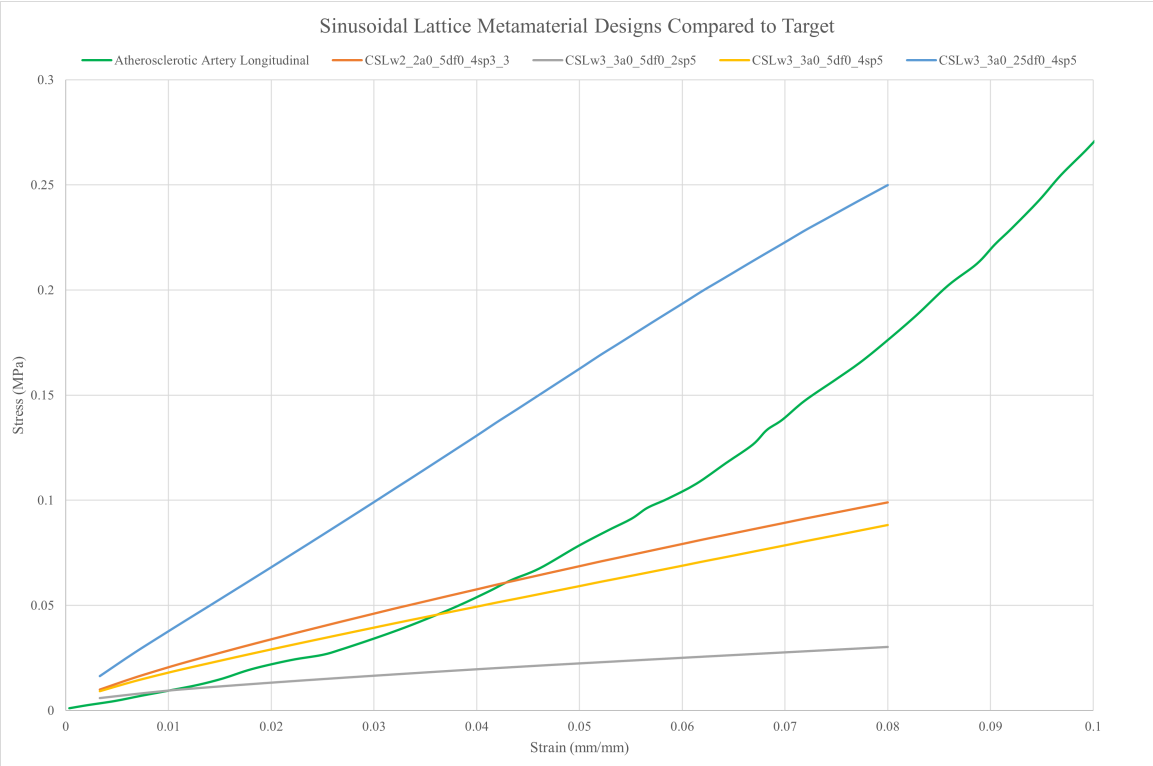

Figure 41: Geometry Tuning Simulations for Complex Sinusoidal Lattice

Figure 42 shows the total deformation of CSLw3_3a0_5df0_4sp5, which was the closest fitting to the target curve. It created little noise on the surface of the structure, with the exception of a slight dimple between lattice sections, however, as it was unable to produce a convex stress-strain curve, this geometry would not be appropriate for use in coronary artery phantoms.

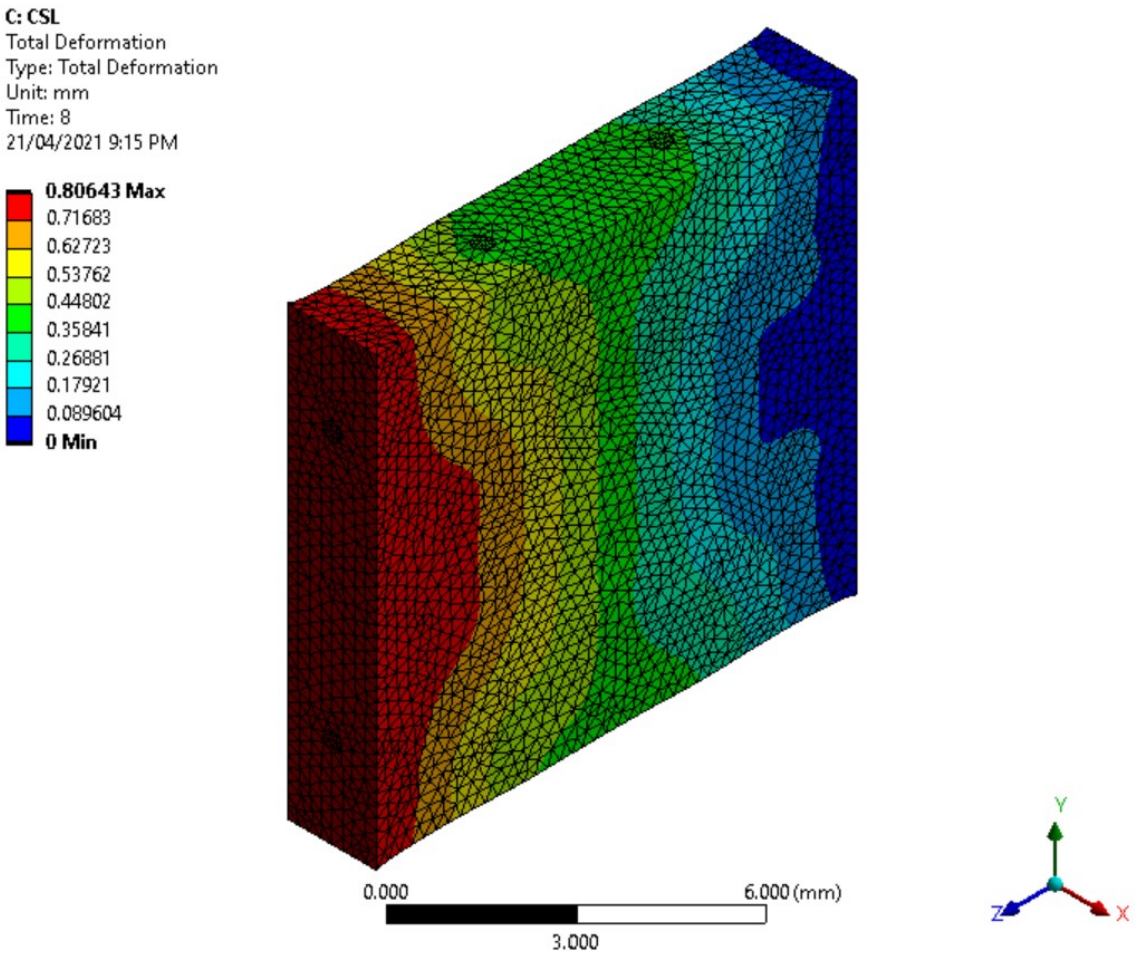

Figure 42: Total Deformation of Final Tuned Complex Sinusoidal Lattice Geometry

4.4.3 Kirigami Spring

In the kirigami spring, the selected tuning parameters were the segment length (length of each loop section in the z-direction), the part height and the fibre diameter. The selected tuning parameters are shown in Table 4. The graph of the results can be seen in Figure 43. Decreasing the segment length and the part height increased the stiffness of the curve, and decreasing fibre diameter decreased the stiffness of the curve. No change in curvature was observed for any tuning parameters selected.

Table 4: Kirigami Spring Tuning Parameters

Name	Segment Length (mm)	Height (mm)	Fibre Diameter (mm)
Base (KSl2_5df0_4h6)	2.5	6	0.4
KSl1_5df0_4h6	1.5	6	0.4
KSl2_5df0_2h6	2.5	6	0.2
KSl2_5df0_4h3	2.5	3	0.4

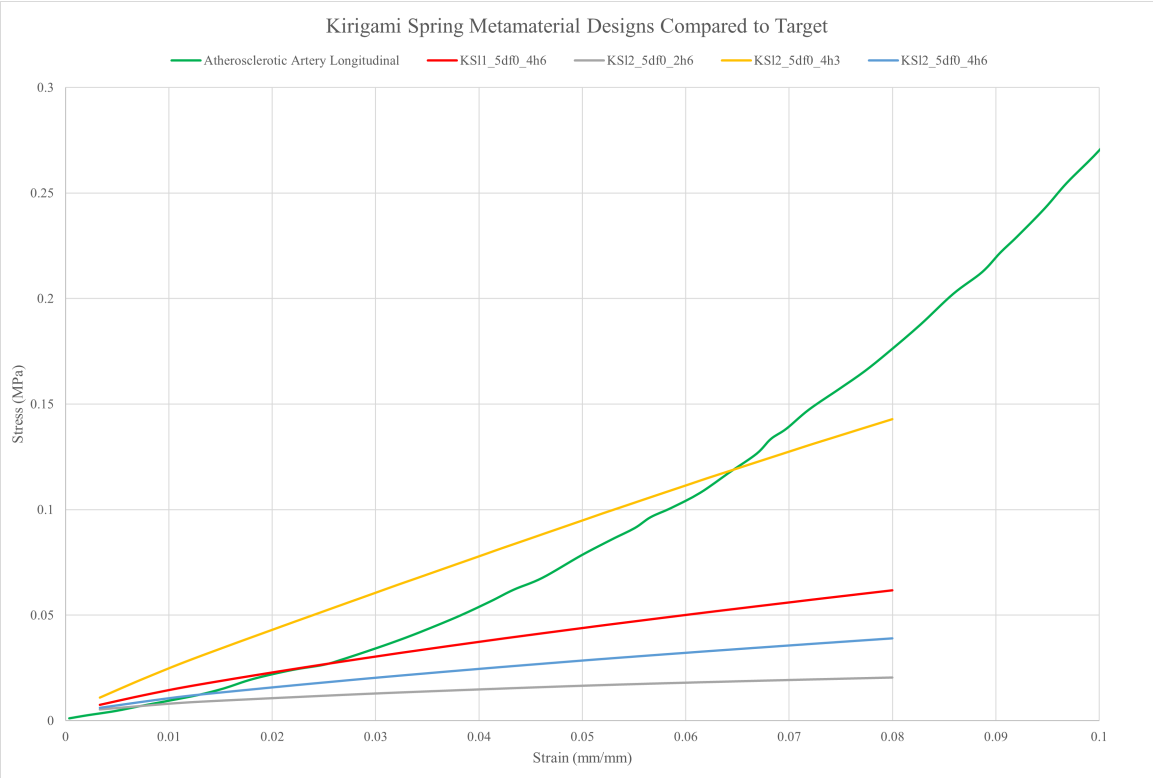

Figure 43: Geometry Tuning Simulations for Kirigami Spring

Figure 44 shows the total deformation of the best fitting kirigami spring geometry, KSl1_5df0_4h6. It created very little deformation perpendicular to the displacement, performing the best out of all geometries investigated in this paper, however as it did not exhibit any strain-stiffening behaviour, it was deemed unsuitable for use in coronary artery phantoms.

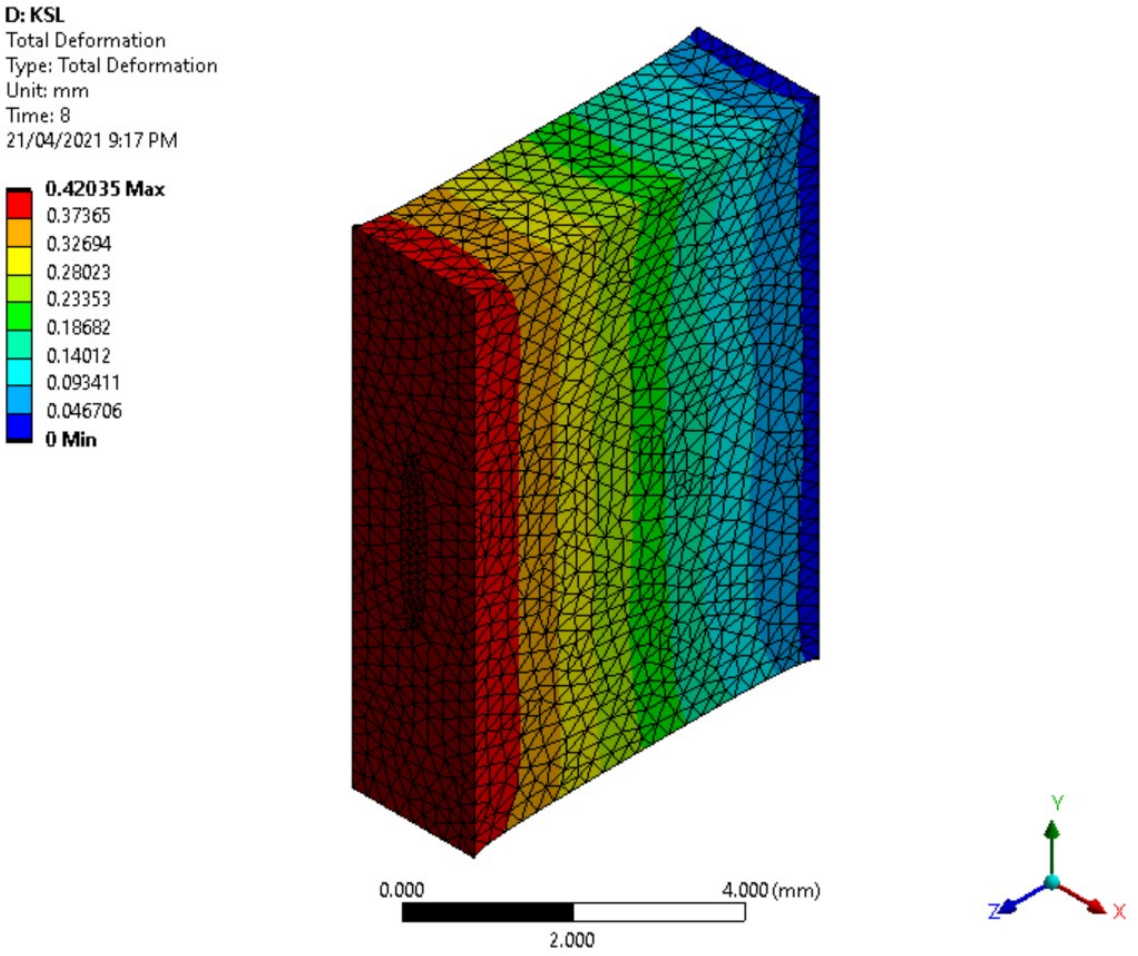

Figure 44: Total Deformation of Final Tuned Kirigami Spring Geometry

4.4.4 Double Helix-Sinusoid Combination

In the double helix-sinusoid combination there were more tuning parameters and combinations that could be changed. These tuning parameters included helical pitch and diameter, the wavelength and amplitude of the sinusoid, the fibre diameter of both structures and the spacing between them. Table 5 shows the combinations of all initial tuning geometries.

Table 5: Double Helix-Sinusoid Combination Tuning Parameters

Name	Double Helix			Sinusoid			Spacing (mm)
	Pitch (mm)	Helical Diam. (mm)	Fibre Diam. (mm)	Wave length (mm)	Amplitude (mm)	Fibre Diam. (mm)	
Base (Helix_p2_5d_f0_2d_h0_7_ Sin_w2_5d_f0_2a0_5_sp2)	2.5	0.7	0.2	2.5	0.5	0.2	2
Helix_p2_5d_f0_2d_h0_7_ Sin_w2_5d_f0_2a0_25_sp2	2.5	0.7	0.2	2.5	0.25	0.2	2
Helix_p2_5d_f0_2d_h1_2_ Sin_w2_5d_f0_2a0_5_sp2	2.5	1.2	0.2	2.5	0.5	0.2	2
Helix_p2_5d_f0_2d_h1_2_ Sin_w2_5d_f0_2a0_25_sp2	2.5	1.2	0.2	2.5	0.25	0.2	2
Helix_p2_5d_f0_2d_h0_7_ Sin_w5d_f0_2a0_5_sp2	2.5	0.7	0.2	5	0.5	0.2	2
Helix_p5d_f0_2d_h0_7_ Sin_w2_5d_f0_2a0_5_sp2	5	0.7	0.2	2.5	0.5	0.2	2
Helix_p5d_f0_2d_h0_7_ Sin_w5d_f0_2a0_5_sp2	5	0.7	0.2	5	0.5	0.2	2
Helix_p2_5d_f0_4d_h0_7_ Sin_w2_5d_f0_2a0_5_sp2	2.5	0.7	0.4	2.5	0.5	0.2	2
Helix_p2_5d_f0_2d_h0_7_ Sin_w2_5d_f0_4a0_5_sp2	2.5	0.7	0.2	2.5	0.5	0.4	2
Helix_p2_5d_f0_4d_h0_7_ Sin_w2_5d_f0_4a0_5_sp2	2.5	0.7	0.4	2.5	0.5	0.4	2
Helix_p2_5d_f0_2d_h0_7_ Sin_w2_5d_f0_2a0_5_sp1	2.5	0.7	0.2	2.5	0.5	0.2	1

Figure 45 shows the impact of varying the spacing between the double helix and sinusoid fibres. It shows that an increased spacing increases the stiffness of the stress-strain curve, however had no influence making a convex curvature.

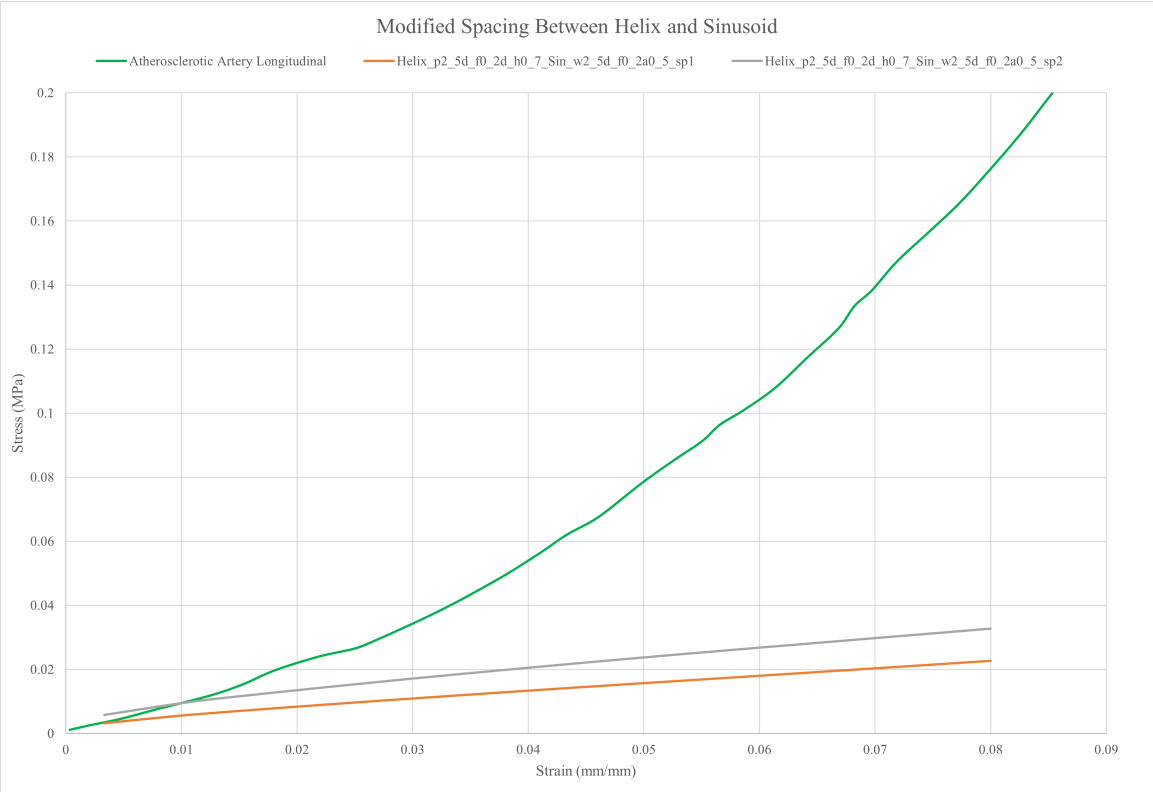

Figure 45: Spacing Geometry Tuning Simulations for Double Helix-Sinusoid Combination

Figure 46 shows the effect of varying the fibre diameters. It can be seen that increasing the fibre diameter in both increases the stiffness of the stress-strain curve, however the helix fibre diameter has a larger effect, likely due to there being two fibres in the structure. There was no convex curvature change observed changing these parameters.

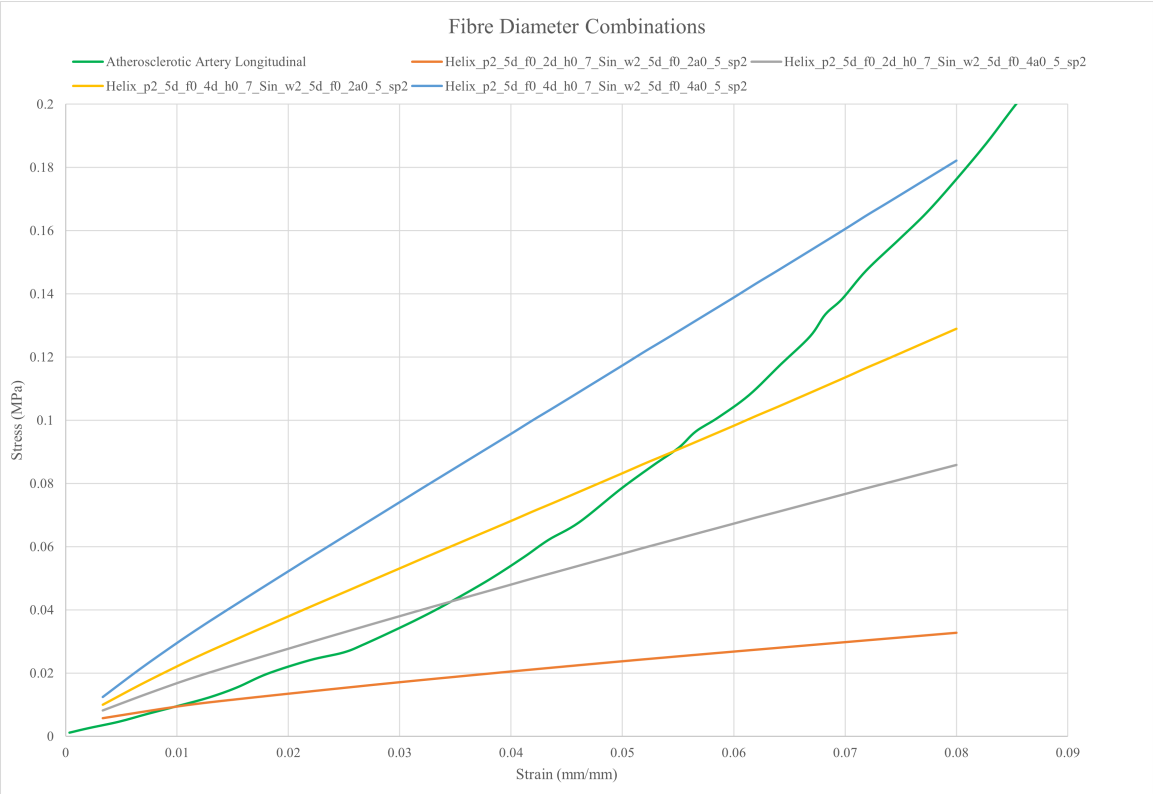

Figure 46: Fibre Diameter Geometry Tuning Simulations for Double Helix-Sinusoid Combination

Figure 47 shows the effect of tuning the helical diameter and amplitude of the sinusoidal wave. Decreasing the amplitude of the sinusoidal wave increased the stiffness of the stress-strain curve, whilst increasing the helical diameter decreased the stiffness. A convex curvature was observed in both simulations with decreased sinusoidal wave amplitude, indicating that this tuning parameter could be utilised to create a more convex curve.

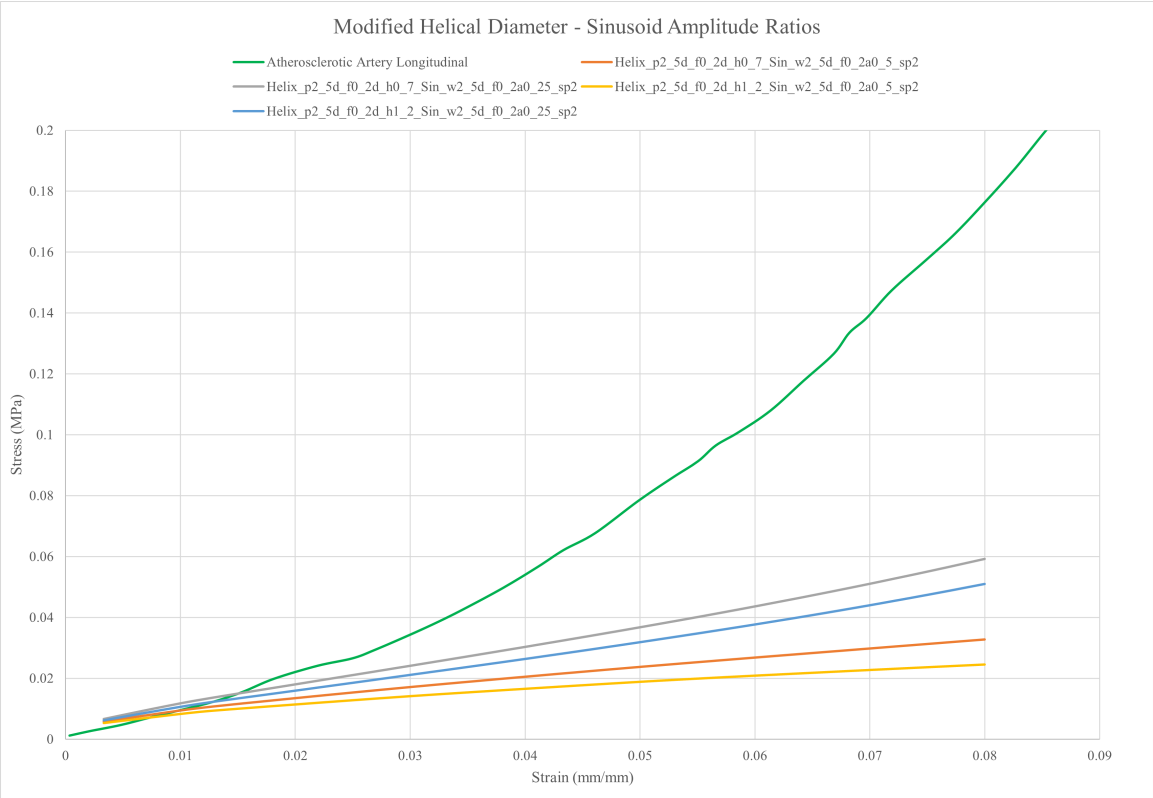

Figure 47: Helix Diameter and Sinusoidal Amplitude Geometry Tuning Simulations for Double Helix-Sinusoid Combination

Figure 48 shows the impact of varying the helical pitch and sinusoidal wavelength. Increasing both the pitch and the wavelength increased the stiffness of the stress-strain curve, with an increased helical pitch having more influence on the stiffness of the curve. Additionally, a significant change in convex curvature was observed in the geometries with the increased helical pitch, indicating that this parameter had a strong influence on the resulting mechanical properties.

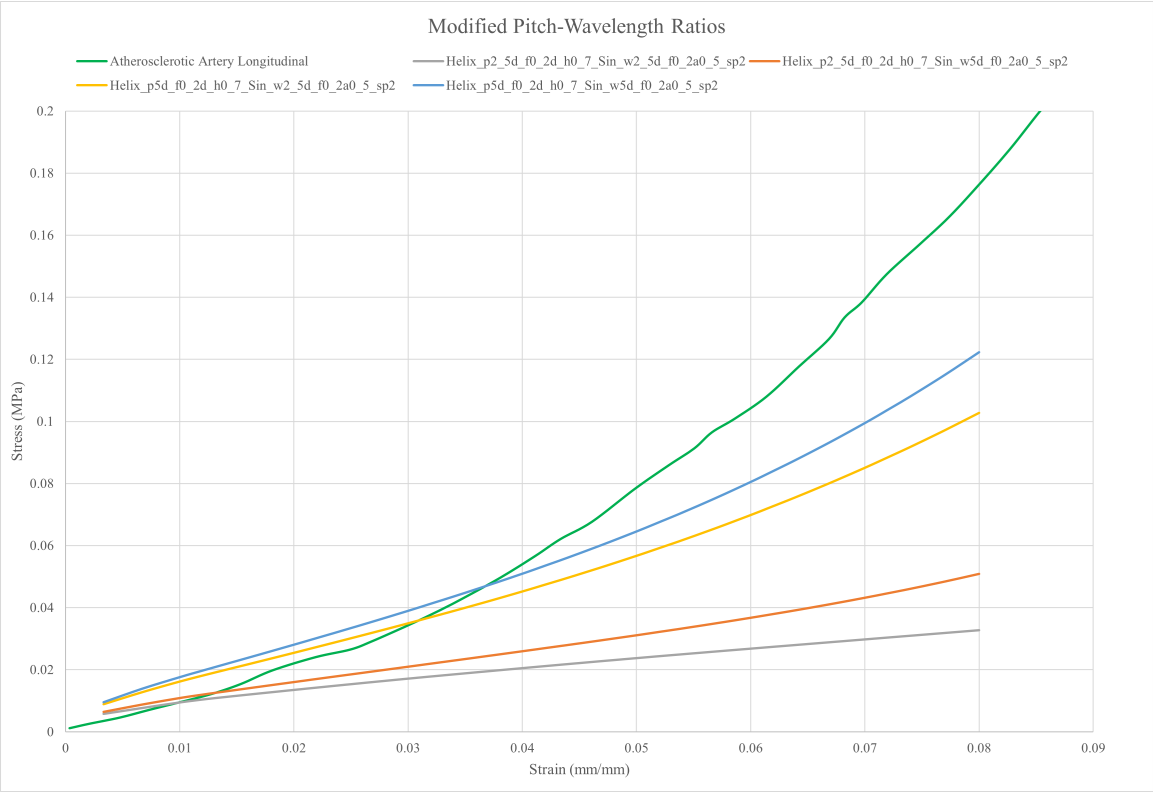

Figure 48: Pitch and Wavelength Geometry Tuning Simulations for Double Helix-Sinusoid Combination

As the double helix-sinusoid combination geometry was the most effective in changing the curvature of the stress-strain graph, it was selected for further tuning, focusing on changing the sinusoidal wavelength and amplitude, and the helical pitch, with varying fibre diameters to control the stiffness of the curve. Figure 49 shows the best curves from the further tuned double helix-sinusoid combination geometries, with Helix_p5d_f0_2d_h1_2_Sin_w4_5d_f0_2 a0_25_sp2 (Double helix: pitch = 5mm, helical diameter = 1.2mm, fibre diameter = 0.2mm. Sinusoidal wave: wavelength = 4.5mm, amplitude = 0.25mm, fibre diameter = 0.2mm. Spacing between fibres = 2mm.) fitting the target curve the best. It closely follows the target curve to strains of 5.5%, which is an improvement on the previously found sinusoidal wave geometries. Additionally, it has a more pronounced convex curve, which is required to better fit the target atherosclerotic coronary artery curve.

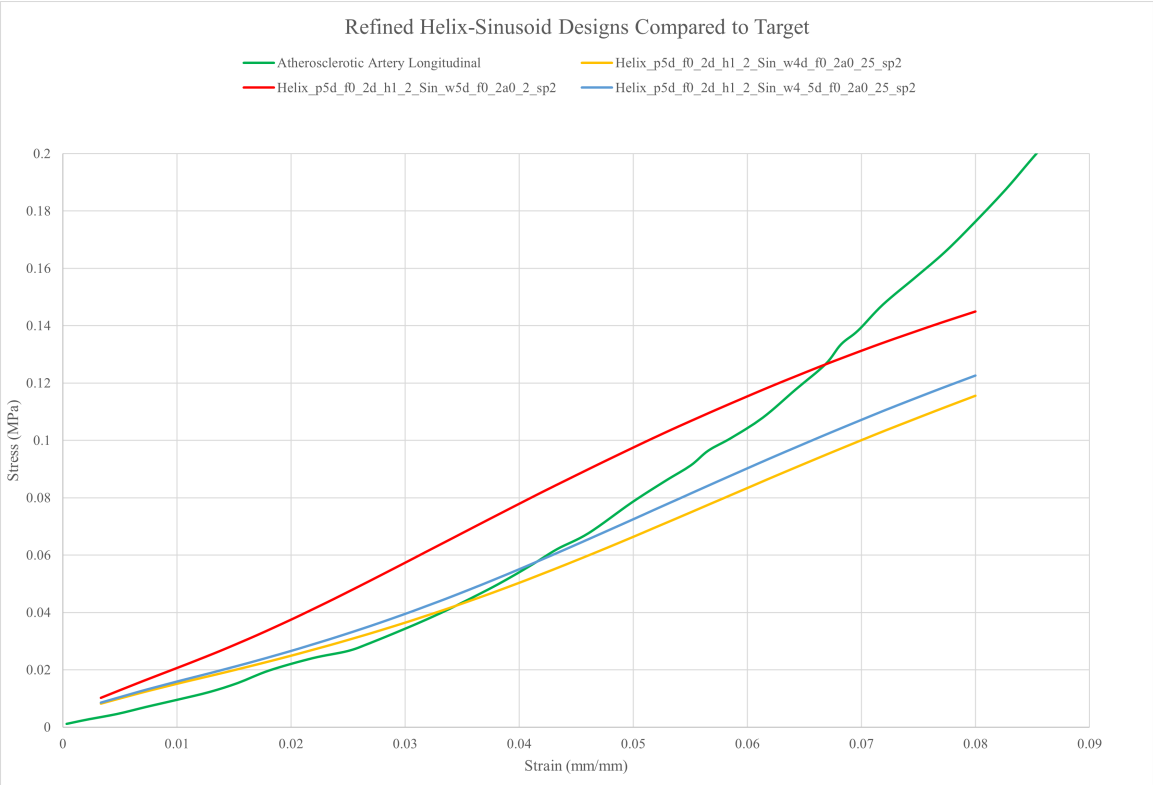

Figure 49: Final Tuned Double Helix-Sinusoid Combination Geometry Stress-Strain Curves

Figure 50 shows the final stress-strain curves from 8% displacement in the circumferential direction. It can be seen that varying geometry has very little influence on the circumferential properties as there was no change between geometries. Additionally, as the target is less stiff than the simulated geometries, and the stress-strain curve is limited by the softest material that can be printed by the 3D printer, it would not be possible to achieve this target curve with the available materials, however it is close enough (within 0.01MPa difference for each strain) to provide a reasonable approximation for the purposes of coronary artery phantoms. It would be an improvement on the current mechanical properties of phantoms available.

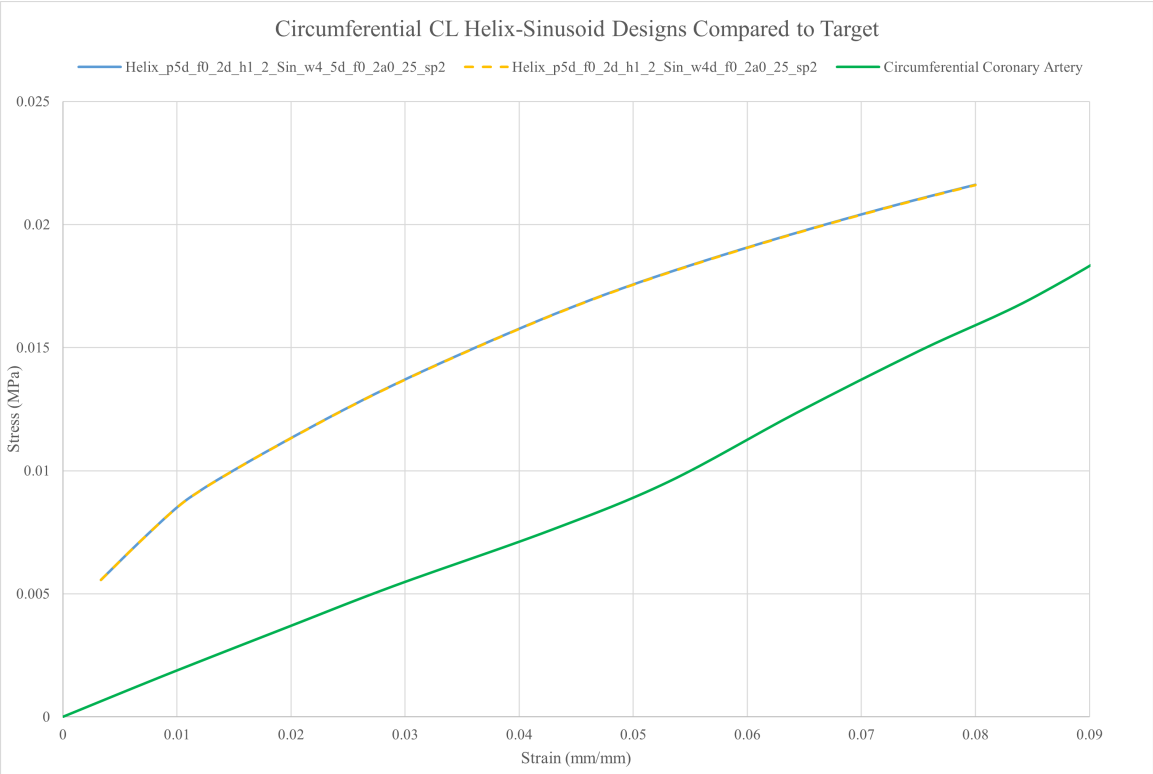

Figure 50: Final Tuned Double Helix-Sinusoid Combination Geometry Stress-Strain Curves in Circumferential Direction

Figure 51 shows a comparison of the final tuned double helix-sinusoid combination geometry with Bautista's best fitting curve (to the target curve established in this paper, not the intima layer of the coronary artery that they used for comparison). The combination geometry clearly shows a better fit to the target curve, especially before strains of 5.5%.

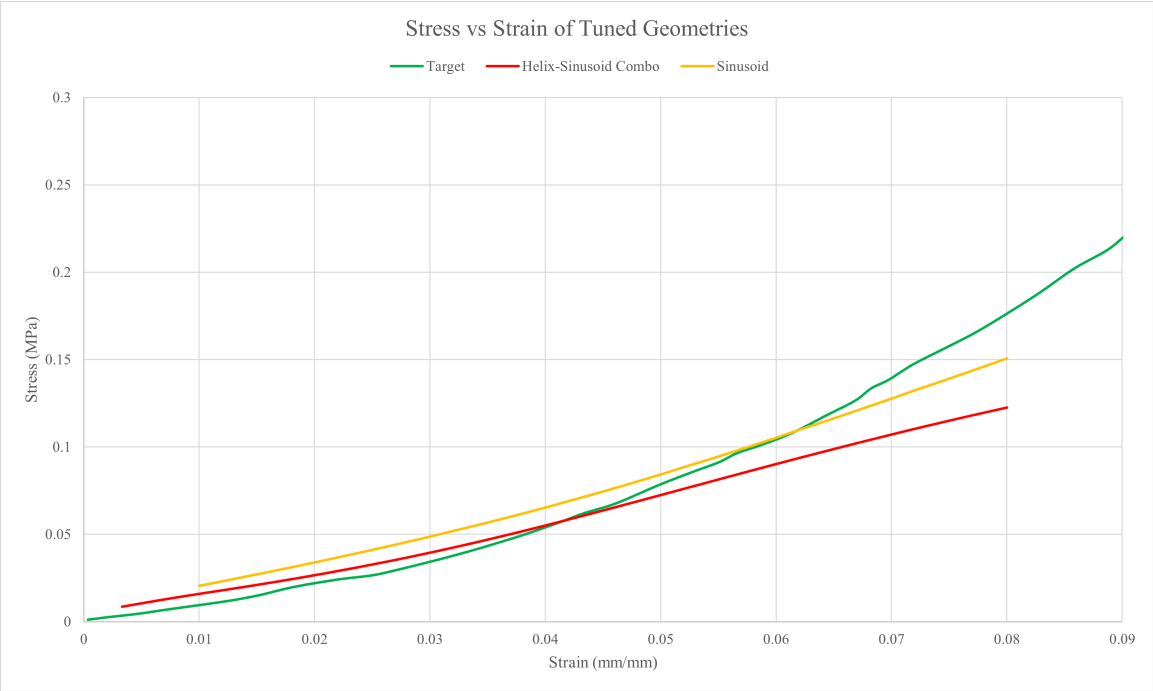

Figure 51: Final Tuned Double Helix-Sinusoid Combination Geometry vs Bautista's Best Fitting Curve[36]

Table 6 shows a comparison of the percentage errors between the final double helix-sinusoid combination and best sinusoidal wave geometries. It reveals that the combination geometry is 11% better overall compared to the sinusoidal wave. It also shows that the combination geometry is has far less error from 0-5% strain than the sinusoidal wave, although it follows the curve less closely after strains of 5%.

Table 6: Comparison of Percentage Error from Target Curve between Final Combination Geometry and Best Sinusoidal Wave

Strain (mm/mm)	Percentage Error Combination	Percentage Error Sinusoidal Wave
1%	67%	115%
2%	21%	55%
3%	15%	42%
4%	2%	17%
5%	8%	0%
6%	14%	5%
7%	23%	13%
8%	30%	18%
Average	22%	33%

Figure 52 shows the total deformation of the final tuned combination geometry. It can be seen that there is little deformation on the x-direction, which is a great improvement on the sinusoidal geometries from previous studies. Additionally, a comparison of the overhead

views of each geometry can be seen in Figures 53 and 54, which highlights the improvements made with this geometry. Figures 55 and 56 show a comparison from the front view, highlighting that significantly less twisting occurs in the combination geometry compared to the sinusoidal wave metamaterial.

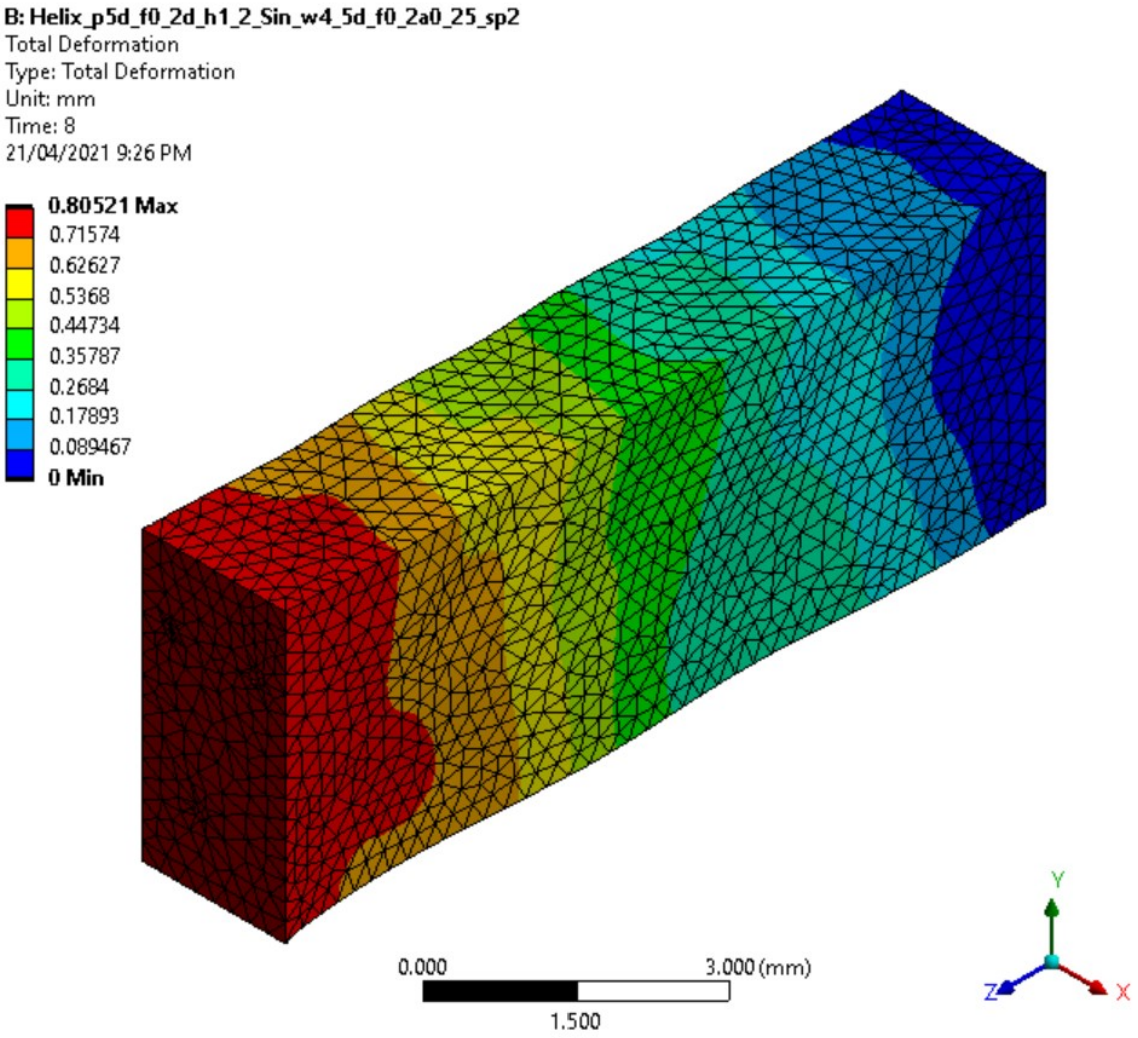

Figure 52: Total Deformation of Final Tuned Double Helix-Sinusoid Combination Geometry

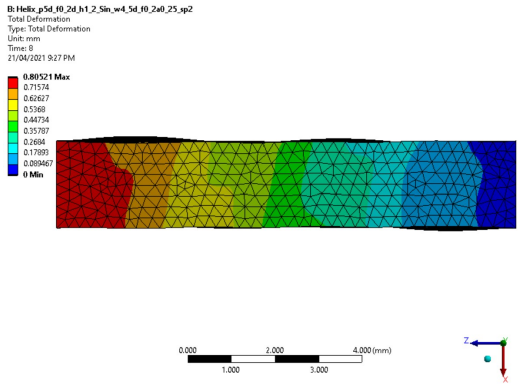

Figure 53: Total Deformation of Final Tuned Double Helix-Sinusoid Combination Geometry from Overhead View

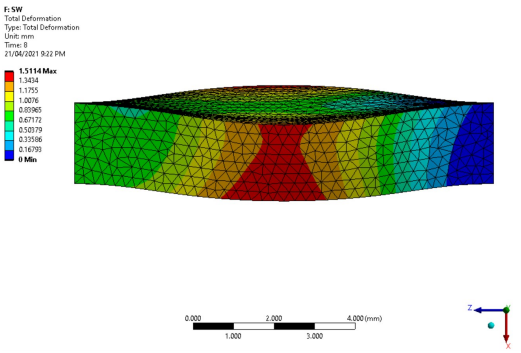

Figure 54: Total Deformation of Bautista's Best Geometry from Overhead View[36]

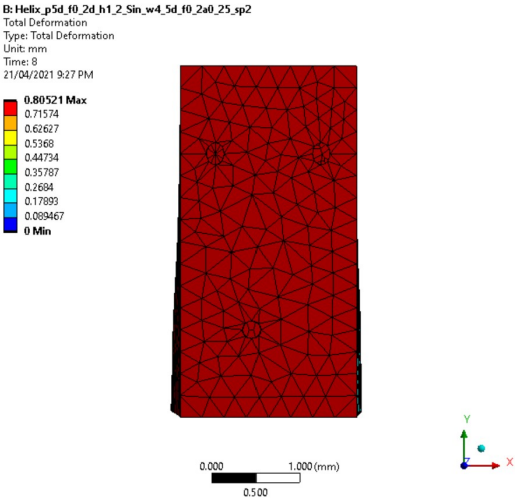

Figure 55: Total Deformation of Final Tuned Double Helix-Sinusoid Combination Geometry from Front View

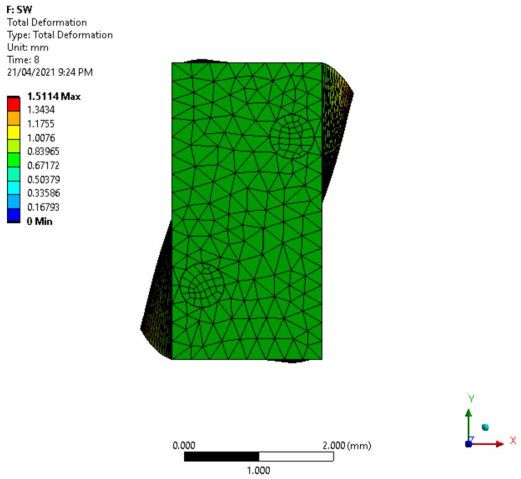

Figure 56: Total Deformation of Bautista's Best Geometry from Front View[36]

4.5 Geometries for 3D Printing and Testing

Finally, the geometries had to be made into CAD and .stl files for 3D printing. Figure 57 shows a 25mm long vessel tube which was generated using the most optimised combination geometry. Figure 58 shows a tensile test strip of the final tuned combination geometry, designed as described by Dizon et al[30] with blocks of CL at each end to prevent excess deformation where the clamps of the universal testing machine hold on. Figures 59 and 60 show the bifurcation geometry that was prepared with the finalised double helix-sinusoid combination metamaterial structure, with a bifurcation angle of 30°.

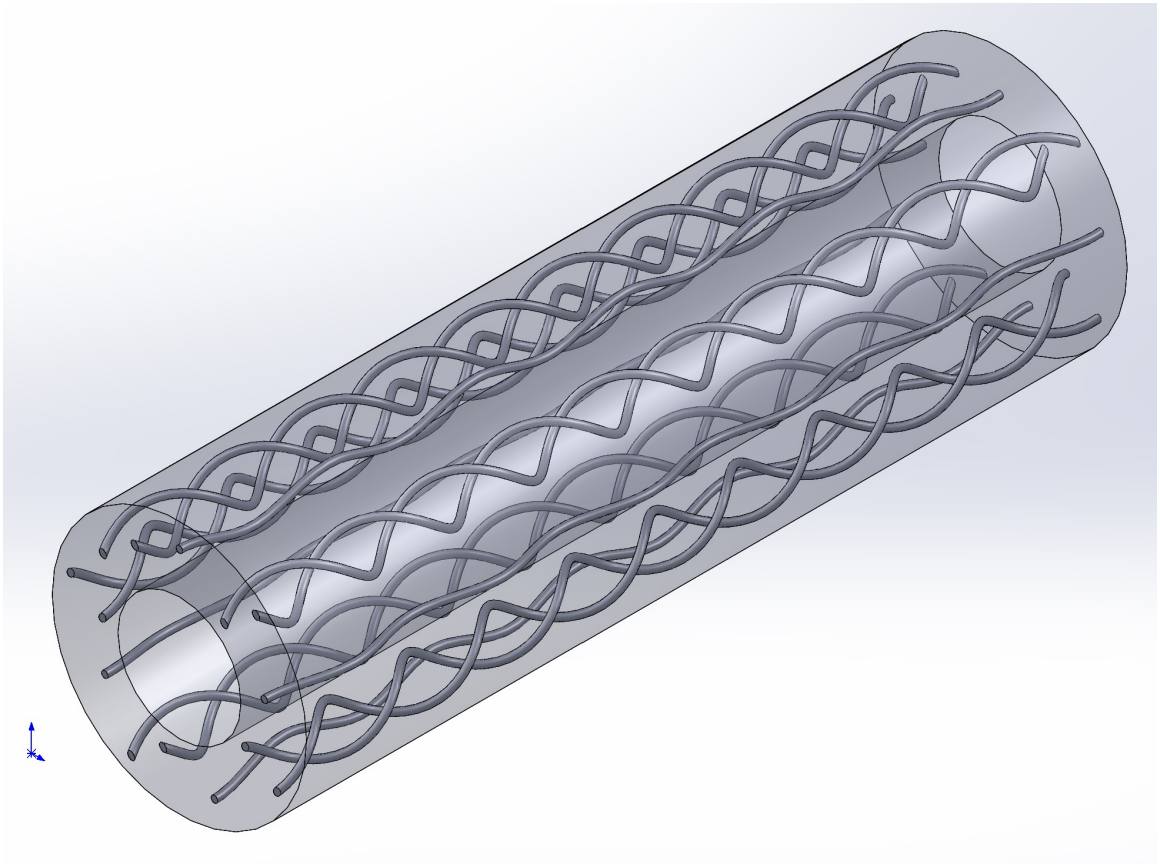

Figure 57: Tube Geometry of Final Tuned Double Helix-Sinusoid Combination Metamaterial

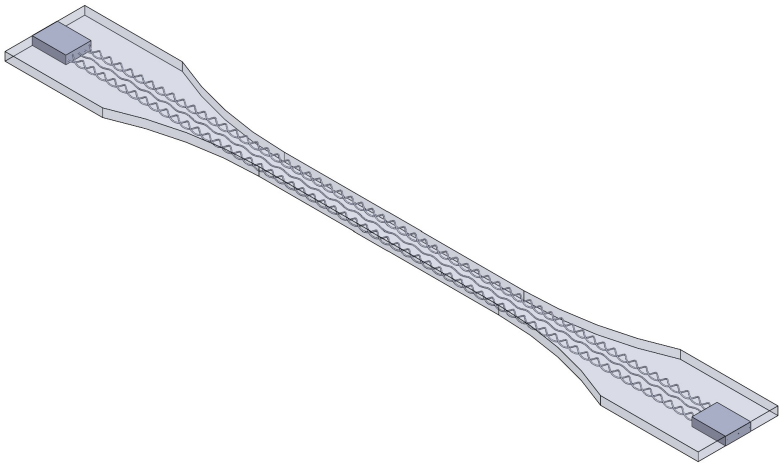

Figure 58: Tensile Test Strip Geometry of Final Tuned Double Helix-Sinusoid Combination Metamaterial

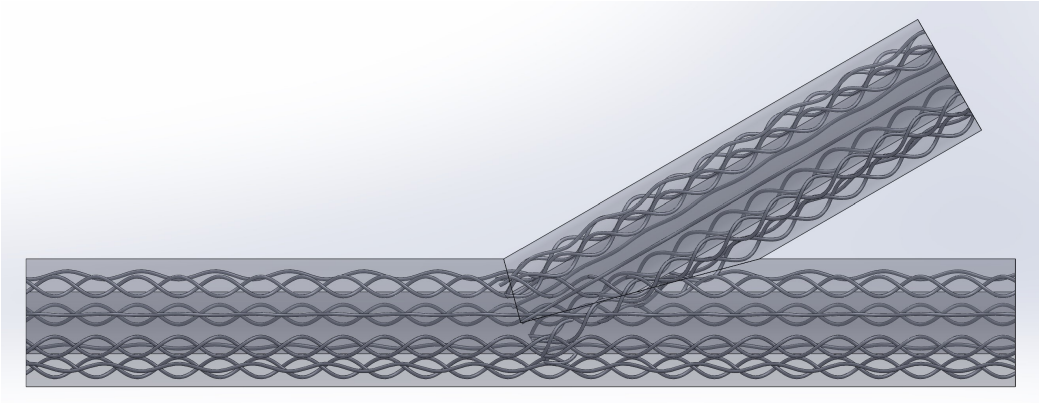

Figure 59: Bifurcation Geometry of Final Tuned Double Helix-Sinusoid Combination Metamaterial Side View

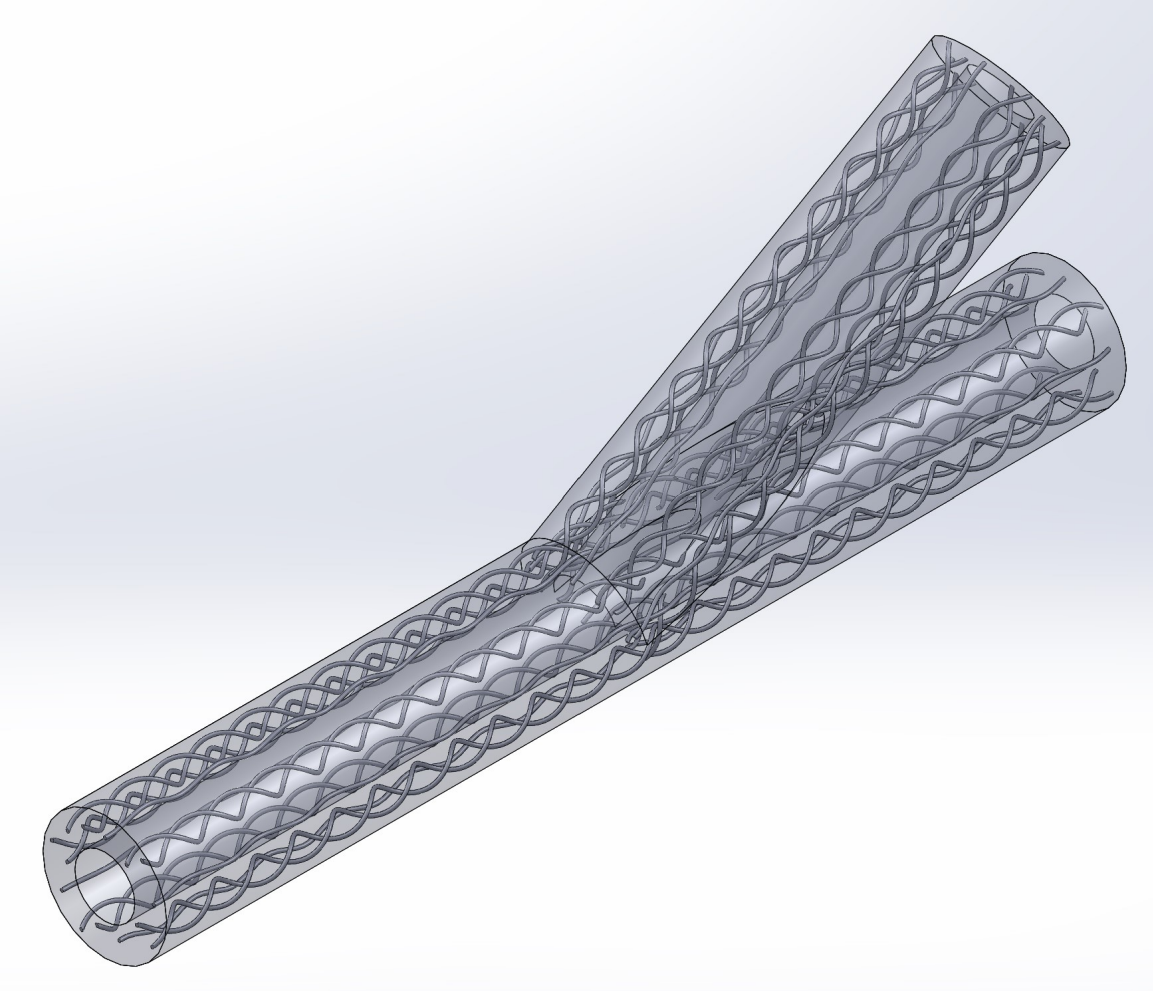

Figure 60: Bifurcation Geometry of Final Tuned Double Helix-Sinusoid Combination Metamaterial Isometric View

Figure 61 shows three preliminary tensile strips (final double helix, complex sinusoidal wave and kirigami spring geometries) and double helix bifurcations which were 3D printed. Unfortunately, these were unable to be tested due to broken and unavailable equipment. It also shows that all of the tensile test strips were printed in the same orientation to ensure no additional variables were added, as discussed by Dizon et al[30]. Figure 62 shows how the geometry of the fibres needed to protrude from the matrix material to be selected for the material to be changed.

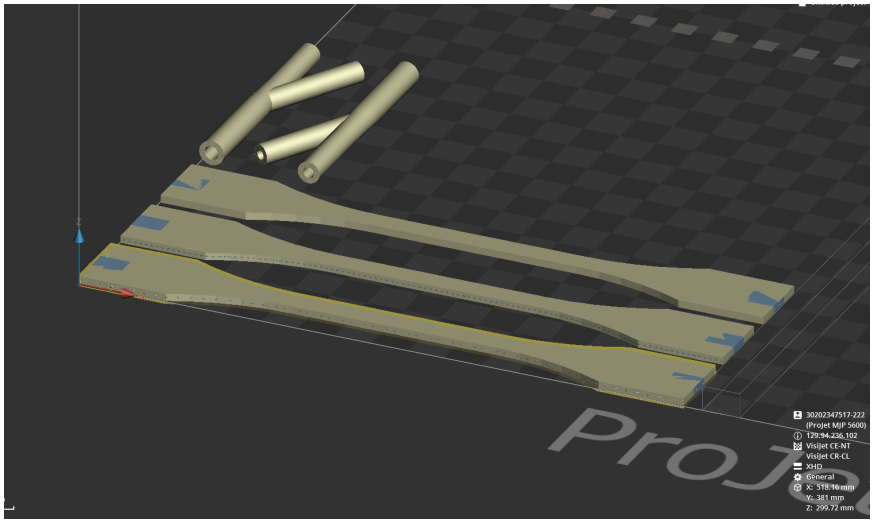

Figure 61: Preliminary Metamaterial Geometries on 3D Printer Bed

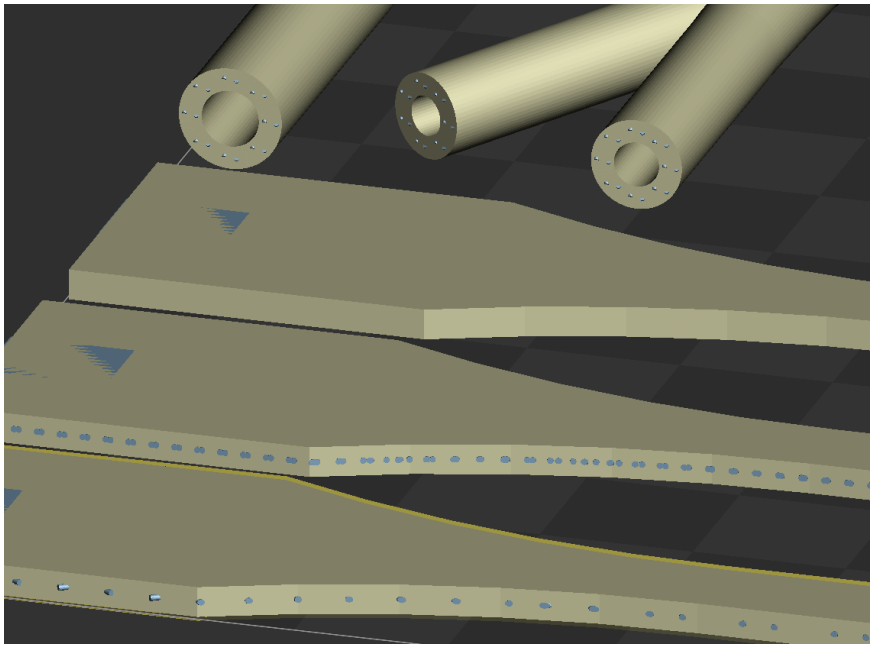

Figure 62: Close Up of Geometries on 3D Printer Bed

5 Discussion and Conclusions

In this section is a discussion of the limitations of this research project, recommendations for next steps and future research and a summary of the findings of this paper.

5.1 Limitations

This project experienced several limitations, the most significant of which was not being able to physically validate the metamaterial simulations by using a universal testing machine to test 3D printed tensile testing strips. This testing would have provided additional validation to the simulations and highlighted any unexpected problems with the geometry, such as delamination occurring before anticipated, or the stiff fibres breaking due to their geometry interacting together. The machines with a small enough load cell that would have been able to test these test strips were broken when the project was at a point where the geometries were ready after testing in simulations. Additionally, machines that were available had load cells that were too large (2kN), which would not have resulted in stress-strain curves with high enough resolution. Furthermore, the 3D printer was broken after the double-helix sinusoid combination had been simulated, and as a result it's tensile test strip and bifurcation could not be 3D printed and tested either.

Another limitation in this project was the available materials. As discussed in Section 4.4.4, the softest material was too stiff to be able to tune any geometries to match the target circumferential data curve. As such, the circumferential direction of the phantom would be too stiff compared to the target curve, although it would have more accurate mechanical properties than existing phantoms available today. Ideally, more materials could be researched to find a soft matrix material which is more suitable to this purpose.

Further limitations of this project include the mechanical properties of the metamaterial changing if the geometry is scaled, meaning that vessels of different sizes and thicknesses would not have the same mechanical properties if the final geometry was used in them. This would become especially problematic at bifurcations of vessels, as fibres join together, or in areas of varying thickness.

Currently, the geometries found in this paper only account for homogeneous materials, however if a vessel is not homogeneous this geometry would not be able to accurately model the artery walls. Phantoms with varying mechanical properties would require further research and investigation.

Additionally, more 3D printed material data would help improve the material models, as it would open up other material models for testing to better approximate the material curve in ANSYS.

Finally, as the 3D printer had to have the internal geometries visible on the exterior of the printed part, this limited the amount of geometries that would be possible to print into a bifurcation. Although it was investigated whether anything could work around this issue, nothing was able to be done due to restrictions with the 3D printer software. Looking into other 3D printers with less restrictive softwares may be prudent to enable the exploration of further geometries.

5.2 Recommendations

In future projects, it is essential to physically test the printed geometries to verify the accuracy of the simulations. This would be done by printing new 3D prints of the geometries created in this paper, as older prints change properties, as described by Dizon et al[30]. The tensile testing strips should be printed and tested with a universal testing machine with a small load cell, and preferably a biaxial measurement device to obtain data about the material behaviour in the circumferential direction under longitudinal tensile loads.

Additionally, a clinician should be consulted about the behaviour of the 3D printed phantoms to see whether they behave appropriately for their uses.

Further investigation into materials, especially the soft matrix material, should be conducted to find a more suitable material which is less stiff than the target circumferential coronary artery curve. This would allow for further tuning in the circumferential direction.

Further research and investigation could be performed into the following areas:

- Methods to smoothly transition between geometries at points of bifurcation.
- Methods to predict the behaviour of scaled geometries to enable variation of size to fit different sized vessels.
- Methods to automate the generation of metamaterial geometry into patient vessel models.
- Investigation into variable pitch and wavelength to vary the mechanical properties along the length of the metamaterial.
- Investigation into whether the cross-section geometry has an impact on the mechanical properties of the metamaterial (i.e. rectangular cross-section instead of circular).
- Investigation into incorporating multiple fibre materials (rather than just CL), which could act like elastin filaments activating at different strains, and may be able to further improve the stress-strain curve.

5.3 Conclusion

The study described in this paper explored the effect of various shaped geometries on the mechanical properties of metamaterials, aimed at replicating the mechanical properties of atherosclerotic coronary arteries. This was done by developing geometries, implementing them into an ANSYS simulation and assessing their stress strain graph. Tuning was performed on double helix, sinusoidal lattice, kirigami spring and double helix-sinusoid combination geometries to identify what geometrical parameters influenced the stress-strain curves of the metamaterials and generate better tuned geometries with convex stress-strain curve which closely followed the target atherosclerotic coronary artery curve.

It was found that the double helix-sinusoid combination geometry was the most effective geometry to tune and match the target curve. The final tuned combination geometry closely followed the target curve up to 5.5% strain, with improvement compared to previous papers. Additionally, the deformation experienced by the metamaterial perpendicular to the displacement was noted to be significantly decreased compared to the previous sinusoidal wave metamaterial which provided the closest approximation before. The perpendicular

deformations in the combination geometry metamaterial were negligible, thus reducing the potential for noise to be developed in any trials or simulations that such a phantom would be used for.

There is great potential for this geometry to be implemented into 3D printed coronary artery phantoms as it much more accurately replicates coronary arteries both geometrically and mechanically, although further research is required to establish how the metamaterial fibres should be integrated into patient specific geometries. Utilising 3D printing will enable phantoms to be created which are more cost effective and patient specific than existing phantoms, whilst integrating a metamaterial geometry will enable the phantom to more accurately replicate the mechanical properties of real coronary arteries.

References

[1] J. Seladi-Schulman. (Feb. 2019). "Arteries of the body," [Online]. Available: https://www.healthline.com/health/arteries-of-the-body. [Accessed August 2020].

[2] K. Wang, C. Wu, Z. Qian, C. Zhang, B. Wang, and M. Vannan, "Dual-material 3d printed metamaterials with tunable mechanical properties for patient-specific tissue-mimicking phantoms," English, *Additive Manufacturing*, vol. 12, no. PA, pp. 31–37, 2016, ISSN: 22148604, [Accessed June 2020].

[3] World Health Organisation. (n.d.). "Cardiovascular diseases (CVDs)," [Online]. Available: https://www.who.int/news-room/fact-sheets/detail/cardiovascular-diseases-(cvds). [Accessed June 2020].

[4] Heart Foundation. (n.d.). "Key statistics: Heart disease in australia," [Online]. Available: https://www.heartfoundation.org.au/about-us/australia-heart-disease-statistics. [Accessed June 2020].

[5] Australian Institute of Health and Welfare. (Jun. 2020). "Cardiovascular disease," [Online]. Available: https://www.aihw.gov.au/reports/heart-stroke-vascular-diseases/cardiovascular-health-compendium/contents/deaths-from-cardiovascular-disease. [Accessed June 2020].

[6] National Heart, Lung and Blood Institute. (n.d.). "Atherosclerosis," [Online]. Available: https://www.nhlbi.nih.gov/health-topics/atherosclerosis#:~:text=Atherosclerosis%5C%20is%5C%20a%5C%20disease%5C%20in,other%5C%20parts%5C%20of%5C%20your%5C%20body.. [Accessed June 2020].

[7] ——, (n.d.). "Heart attack," [Online]. Available: https://www.nhlbi.nih.gov/health-topics/heart-attack#:~:text=A%5C%20heart%5C%20attack%5C%20happens%5C%20if,result%5C%20of%5C%20ischemic%5C%20heart%5C%20disease.. [Accessed June 2020].

[8] Heart Foundation. (n.d.). "What is coronary heart disease?" [Online]. Available: https://www.heartfoundation.org.au/conditions/coronary-heart-disease. [Accessed June 2020].

[9] American Heart Association. (Jul. 2015). "Coronary artery disease - coronary heart disease," [Online]. Available: https://www.heart.org/en/health-topics/consumer-healthcare/what-is-cardiovascular-disease/coronary-artery-disease. [Accessed June 2020].

[10] Centers for Disease Control and Prevention. (Dec. 2019). "Coronary artery disease (cad)," [Online]. Available: https://www.cdc.gov/heartdisease/coronary_ad.htm. [Accessed June 2020].

[11] UCSF Department of Surgery. (2020). "Coronary artery disease," [Online]. Available: https://surgery.ucsf.edu/conditions--procedures/coronary-artery-disease.aspx. [Accessed June 2020].

[12] T. Doenst, A. Haverich, P. Serruys, R. O. Bonow, P. Kappetein, V. Falk, E. Velazquez, A. Diegeler, and H. Sigusch, "Pci and cabg for treating stable coronary artery disease," *Journal of the American College of Cardiology*, vol. 73, no. 8, pp. 964–976, 2019, ISSN: 0735-1097. DOI: 10.1016/j.jacc.2018.11.053. [Online]. Available: https://www.onlinejacc.org/content/73/8/964, [Accessed June 2020].

[13] National Institute of Standards and Technology. (Apr. 2019). "What are imaging phantoms?" [Online]. Available: https://www.nist.gov/topics/physics/what-are-imaging-phantoms. [Accessed June 2020].

[14] J. Singh, J. Depta, and Y. Patel. (2017). "Bifurcation lesions," [Online]. Available: https://www.thecardiologyadvisor.com/home/decision-support-in-medicine/cardiology/bifurcation-lesions/#:~:text=The%5C%20European%5C%20Bifurcation%5C%20Club%5C%20defines,to%5C%20characterize%5C%20coronary%5C%20bifurcation%5C%20lesions.. [Accessed August 2020].

[15] A. Latib and A. Colombo, "Bifurcation disease: What do we know, what should we do?" *JACC: Cardiovascular Interventions*, vol. 1, no. 3, pp. 218–226, 2008, ISSN: 1936-8798. DOI: https://doi.org/10.1016/j.jcin.2007.12.008. [Online]. Available: http://www.sciencedirect.com/science/article/pii/S1936879808001684, [Accessed August 2020].

[16] G. A. Holzapfel, G. Sommer, C. T. Gasser, and P. Regitnig, "Determination of layer-specific mechanical properties of human coronary arteries with nonatherosclerotic intimal thickening and related constitutive modeling," eng, *American journal of physiology. Heart and circulatory physiology*, vol. 289, no. 5, H2048, 2005, ISSN: 0363-6135, [Accessed August 2020].

[17] A. Karimi, S. M. Rahmati, T. Sera, S. Kudo, and M. Navidbakhsh, "A combination of experimental and numerical methods to investigate the role of strain rate on the mechanical properties and collagen fiber orientations of the healthy and atherosclerotic human coronary arteries," *Bioengineered*, vol. 8, no. 2, pp. 154–170, 2017, ISSN: 2165-5979. DOI: 10.1080/21655979.2016.1212134. [Online]. Available: https://dx.doi.org/10.1080/21655979.2016.1212134.

[18] M. H. Kural, M. Cai, D. Tang, T. Gwyther, J. Zheng, and K. L. Billiar, "Planar biaxial characterization of diseased human coronary and carotid arteries for computational modeling," *Journal of Biomechanics*, vol. 45, no. 5, pp. 790–798, 2012, ISSN: 0021-9290. DOI: 10.1016/j.jbiomech.2011.11.019. [Online]. Available: https://dx.doi.org/10.1016/j.jbiomech.2011.11.019.

[19] K. Khanafer, M. Schlicht, and R. Berguer, "How should we measure and report elasticity in aortic tissue?" *European Journal of Vascular and Endovascular Surgery*, vol. 45, no. 4, pp. 332–339, 2013, ISSN: 1078-5884. DOI: 10.1016/j.ejvs.2012.12.015. [Online]. Available: https://dx.doi.org/10.1016/j.ejvs.2012.12.015.

[20] A. Karimi, M. Navidbakhsh, A. Shojaei, and S. Faghihi, "Measurement of the uniaxial mechanical properties of healthy and atherosclerotic human coronary arteries," *Materials Science and Engineering: C*, vol. 33, no. 5, pp. 2550–2554, 2013, ISSN: 0928-4931. DOI: 10.1016/j.msec.2013.02.016.

[21] G. A. Holzapfel, G. Sommer, and P. Regitnig, "Anisotropic mechanical properties of tissue components in human atherosclerotic plaques," eng, *Journal of biomechanical engineering*, vol. 126, no. 5, p. 657, 2004, ISSN: 0148-0731, [Accessed August 2020].

[22] A. C. Akyildiz, C.-K. Chai, C. W. J. Oomens, A. van Der Lugt, F. P. T. Baaijens, G. J. Strijkers, and F. J. H. Gijsen, "3d fiber orientation in atherosclerotic carotid plaques," eng, *Journal of structural biology*, vol. 200, no. 1, p. 28, 2017, ISSN: 1047-8477, [Accessed August 2020].

[23] C.-K. Chai, A. C. Akyildiz, L. Speelman, F. J. H. Gijsen, C. W. J. Oomens, M. R. H. M. van Sambeek, A. van Der Lugt, and F. P. T. Baaijens, "Local anisotropic mechanical properties of human carotid atherosclerotic plaques - characterisation by microindentation and inverse finite element analysis," eng, *Journal of the mechanical behavior of biomedical materials*, vol. 43, p. 59, 2015, ISSN: 1878-0180, [Accessed August 2020].

[24] A. Hipper and G. Isenberg, "Cyclic mechanical strain decreases the dna synthesis of vascular smooth muscle cells," English, *Pflügers Archiv - European Journal of Physiology*, vol. 440, no. 1, pp. 19–27, May 2000, Copyright - Springer-Verlag 2000; Last updated - 2014-08-02. [Online]. Available: https://login.wwwproxy1.library.unsw.edu.au/login?qurl=https%5C%3A%5C%2F%5C%2Fwww.proquest.com%5C%2Fscholarly-journals%5C%2Fcyclic-mechanical-strain-decreases-dna-synthesis%5C%2Fdocview%5C%2F874023910%5C%2Fse-2%5C%3Faccountid%5C%3D12763.

[25] K. Wang, C. Ho, C. Zhang, and B. Wang, "A review on the 3d printing of functional structures for medical phantoms and regenerated tissue and organ applications," English, *Engineering*, vol. 3, no. 5, pp. 653–662, 2017, ISSN: 2095-8099, [Accessed June 2020].

[26] J. Brunette, R. Mongrain, J. Laurier, R. Galaz, and J. C. Tardif, "3d flow study in a mildly stenotic coronary artery phantom using a whole volume piv method," eng, *Medical engineering physics*, vol. 30, no. 9, p. 1193, 2008, ISSN: 1350-4533, [Accessed August 2020].

[27] V. Filippou and C. Tsoumpas, "Recent advances on the development of phantoms using 3d printing for imaging with ct, mri, pet, spect, and ultrasound," *Medical Physics*, vol. 45, no. 9, e740–e760, 2018, ISSN: 0094-2405, [Accessed July 2020].

[28] G. Biglino, P. Verschueren, R. Zegels, A. M. Taylor, and S. Schievano, "Rapid prototyping compliant arterial phantoms for in-vitro studies and device testing," eng, *Journal of cardiovascular magnetic resonance*, vol. 15, no. 1, p. 2, 2013, ISSN: 1097-6647. [Online]. Available: https://doaj.org/article/0aa1abb4cc374a83a8a0964120c1d709, [Accessed July 2020].

[29] S. Yazdi, P. Geoghegan, P. Docherty, M. Jermy, and A. Khanafer, "A review of arterial phantom fabrication methods for flow measurement using piv techniques," eng, *Annals of Biomedical Engineering*, vol. 46, no. 11, pp. 1697–1721, 2018, ISSN: 0090-6964, [Accessed August 2020].

[30] J. Dizon, A. Espera, Q. Chen, and R. Advincula, "O mechanical characterization of 3d-printed polymers," English, *Additive Manufacturing*, vol. 20, pp. 44–67, 2018, ISSN: 2214-8604, [Accessed July 2020].

[31] M. Toepker, G. Euller, E. Unger, M. Weber, D. Kienzl, C. J. Herold, and H. Ringl, "Stenosis quantification of coronary arteries in coronary vessel phantoms with second-generation dual-source ct: Influence of measurement parameters and limitations," eng, *AJR. American journal of roentgenology*, vol. 201, no. 2, W227, 2013, ISSN: 0361-803X, [Accessed July 2020].

[32] A. J. Cloonan, D. Shahmirzadi, R. X. Li, B. J. Doyle, E. E. Konofagou, and T. M. Mcgloughlin, "3d-printed tissue-mimicking phantoms for medical imaging and computational validation applications," eng, *3D printing and additive manufacturing*, vol. 1, no. 1, p. 14, 2014, ISSN: 2329-7662, [Accessed July 2020].

[33] Z. Qian, K. Wang, S. Liu, X. Zhou, V. Rajagopal, C. Meduri, J. R. Kauten, Y.-H. Chang, C. Wu, C. Zhang, B. Wang, and M. A. Vannan, "Quantitative prediction of paravalvular leak in transcatheter aortic valve replacement based on tissue-mimicking 3d printing," eng, *JACC. Cardiovascular imaging*, vol. 10, no. 7, p. 719, 2017, ISSN: 1876-7591, [Accessed July 2020].

[34] J. U. Surjadi, L. Gao, H. Du, X. Li, X. Xiong, N. X. Fang, and Y. Lu, "Mechanical metamaterials and their engineering applications," *Advanced Engineering Materials*, vol. 21, no. 3, p. 1 800 864, 2019. DOI: 10.1002/adem.201800864. eprint: https://onlinelibrary.wiley.com/doi/pdf/10.1002/adem.201800864. [Online]. Available: https://onlinelibrary.wiley.com/doi/abs/10.1002/adem.201800864, [Accessed July 2020].

[35] K. Wang, Y. Zhao, Y. Chang, Z. Qian, C. Zhang, B. Wang, M. Vannan, and M. Wang, "Controlling the mechanical behavior of dual-material 3d printed meta-materials for patient-specific tissue-mimicking phantoms," English, *Materials Design*, vol. 90, pp. 704–712, 2016, ISSN: 0264-1275, [Accessed June 2020].

[36] F. Bautista, "3d printing realistic coronary arterial replicas," Fernan Bautista's Thesis Report submitted to UNSW, Nov. 2019, [Accessed June 2020].

[37] N. Karathanasopoulos, H. Reda, and J. Ganghoffer, "Designing two-dimensional metamaterials of controlled static and dynamic properties," English, *Computational Materials Science*, vol. 138, pp. 323–332, 2017, ISSN: 0927-0256, [Accessed July 2020].

[38] H. Jiang, Z. Zhang, and Y. Chen, "3d printed tubular lattice metamaterials with engineered mechanical performance," *Applied Physics Letters*, vol. 117, no. 1, p. 011 906, 2020, ISSN: 0003-6951. DOI: 10.1063/5.0014932.

[39] Y. Chen, T. Li, F. Scarpa, and L. Wang, "Lattice metamaterials with mechanically tunable poisson's ratio for vibration control," *Physical Review Applied*, vol. 7, no. 2, 2017, ISSN: 2331-7019. DOI: 10.1103/physrevapplied.7.024012.

[40] Y. Zhang, F. Zhang, Z. Yan, Q. Ma, X. Li, Y. Huang, and J. A. Rogers, "Printing, folding and assembly methods for forming 3d mesostructures in advanced materials," *Nature Reviews Materials*, vol. 2, no. 4, p. 17 019, 2017, ISSN: 2058-8437. DOI: 10.1038/natrevmats.2017.19.

[41] B. Kim, S. Lee, J. Lee, S. Cho, H. Park, S. Yeom, and S. Park, "A comparison among neo-hookean model, mooney-rivlin model, and ogden model for chloroprene rubber," eng, *International Journal of Precision Engineering and Manufacturing*, vol. 13, no. 5, pp. 759–764, 2012, ISSN: 2234-7593, [Accessed August 2020].

A Resources and Training

Table 7: Required Resources for Project

Resource	Description
SolidWorks 2019-2020	3D modelling software
ANSYS 2020 R1	FEA software
Existing FEA models	FEA models from previous thesis work
3D Printed Polymer Data	Stress-strain data of 3D printer polymers for implementation into ANSYS
Projet MJP 5600	3D Systems polyjet technology 3D printer, located in J18, Willis Annexe Room 106, UNSW
VisiJet CR-CL 200	Rigid 3D printer polymer
VisiJet CE-NT	Elastomeric 3D printer polymer
3D Sprint	3D printer management software, installed on
Autodesk Meshmixer	3D model mesh management and 3D print optimisation software
Instron 3369	2kN universal testing machine, located in J18, Willis Annexe, Room 102, UNSW

Table 8: Required Training for Project

Training	Description
SolidWorks training	Multiple resources and guides were available online to facilitate software training, as well as UNSW courses.
ANSYS training	Multiple resources and guides were available online to facilitate software training, as well as UNSW courses.
3D printer training	Resources were provided to guide through the 3D printing process. Technical officers were also able to provide assistance.
Instron 3369 training	Training and induction for this machine was conducted with Mr Seetha Mahadevan.
Willis Annexe lab induction	Several online training courses and a physical induction were conducted before access to labs was permitted.